Offshore and ~~O~~onshore ~~P~~power curve characterization for ground-generation ~~AWES~~ airborne wind energy systems

Markus Sommerfeld[1], Martin Dörenkämper[2], Jochem De Schutter[3], and Curran Crawford[1]

[1]Institute for Integrated Energy Systems, University of Victoria,British Columbia, Canada
[2]Fraunhofer Institute for Wind Energy Systems (IWES), Oldenburg, Germany
~~[2]~~ [3]Systems Control and Optimization Laboratory IMTEK, University of Freiburg, Germany

Correspondence: Markus Sommerfeld (msommerf@uvic.ca)

Abstract. Airborne wind energy systems (AWESs) are ~~nominally~~ envisaged to operate at altitudes above conventional wind turbines (WTs) and harvest energy from stronger winds aloft. This study investigates typical flight trajectories, operating heights, power curves and annual energy production (AEP) of a ground-generation AWES with a wing area of $A_{\text{wing}} = 20\text{m}^2$. Various companies and researchers have proposed power curve characterizations for AWES~~, but no~~ and a first consensus for an industry-wide standard has been reached. A universal description of a ground-generation AWES power curve is difficult to define, because determining a meaningful reference wind speed at reference height is difficult and can vary significantly between designs. ~~of complex tether and misalignment (cosine) losses subject to alternating flight paths and wind conditions, which lead to significant changes in the average cycle power. This study determines AWES power and AEP based on the `awebox` optimal control model driven by representative onshore and offshore wind data.~~ 10-minute mesoscale onshore and offshore wind conditions are analyzed and categorized with respect to atmospheric stability as well as annual and diurnal variation. ~~To reduce computational costs, these wind data are categorized using k-means clustering.~~ Wind data are categorized using k-means clustering, to reduce computational cost This study determines power and AEP based on the `awebox` optimal control model driven by representative onshore and offshore wind data with various numbers of clusters. The derived vertical profiles cover a wide range of wind speeds and profile shapes which can not be replicated by standard logarithmic wind speed profiles. Wind data drives the optimization and result in distinct optimal ~~AWES~~ trajectories and power cycles.

Our data shows that optimal ~~AWES~~ operating heights are generally below 400 m and mostly around 200 m. We compare ~~AWES~~ power curve descriptions and estimate AEP based on wind speed probability distributions over various reference heights. These results are compared to quasi steady-state (~~QSS~~ QSM) AWES and WT reference models. The optimized power curves show a ~~delay in rated wind speed~~ a higher rated wind speed which can be attributed to increased tether losses which are not captured by the simplified model. Offshore AEP is generally higher than onshore, but lower wind shear weakens the argument for higher operating altitudes for AWES compared to conventional WT.

1 Introduction

Airborne wind energy systems (AWESs) aspire to harvest stronger and less turbulent winds at mid-altitude, here defined as heights above 100 m and below 1500 m, nominally beyond what is achievable with conventional wind turbines (WTs). The

prospects of higher energy yield combined with reduced capital cost motivate the development of this novel class of renewable energy technology (Lunney et al., 2017; Fagiano and Milanese, 2012). Unlike conventional WTs, which over the last decades have converged to a single concept with three blades and a conical tower, several different AWES concepts and designs are still under investigation by numerous companies and research institutes (Cherubini et al., 2015). These kite-inspired systems consist of three main components: one or more flying wings or kites, one or more ground stations and one or more tethers to connect them. This study focuses on the two-phase, ground-generation concept, also referred to as pumping-mode, which is the main concept that industry is currently investigating. During the reel-out phase the wing pulls a non-conductive tether from a drum on the ground which is connected to a generator, thereby producing electricity. This is then followed by the reel-in phase during which the wing adjusts its angle of attack to reduce aerodynamic forces and returns to its initial position. Various other concepts such as fly-gen, aerostat or rotary lift are not within the scope of this study (Cherubini et al., 2015).

Since this technology is still at an early stage of development, validation and comparison of results is difficult. A standardized power curve definition would enable comparison between different AWES concepts and to conventional wind turbines. Recent consensus among the AWES community defined the reference height as the pattern trajectory height, which is the expected or actual time-averaged height during the reel-out (power production) phase (Airborne Wind Europe, 2021). Together with the site-specific wind resource, power curves help wind park planners and AWES device manufacturers to estimate annual energy production (AEP) and determine financial viability (Malz et al., 2020). Note that the wind data used to derive the AEP estimates are not fully~~,~~ in accordance with wind resource assessment guidelines which typically recommend multi-year wind measurements and long-term wind data corrections via simulations. All statements made in this research only apply to the investigated time periods and locations which are assumed to be reasonable representative of wind profiles that would be encountered during operation (Section 2). ~~As such t~~This work supports the development and implementation of this novel technology by proposing a methodology to estimate power and energy generation based on a small set of realistic wind conditions. In contrast to a conventional WT, the power output of an AWES is highly dependent on the complete wind speed profile (wind speed and direction variation with height) as system performance is governed by optimal operating trajectories over the wind profile altitude range rather than primarily by a hub-height wind speed. Simple wind profile approximations using logarithmic or exponential wind speed profiles, which are often erroneously applied beyond earths surface layer (Optis et al., 2016), might approximate long-term average conditions, but can not capture the broad variation of profile shapes that exist on short timescales (Emeis, 2013). They are therefore an inappropriate approximation to estimate instantaneous, diurnal and seasonal variation in electrical power output. However, they are the standard in most AWES power estimation studies. Leuthold et al. (2018) investigated the power-optimal trajectories and performance of a ground-generation multiple-kite AWES over a range of logarithmic wind speed profiles, with different reference wind speeds. ~~In~~ Licitra et al. (2019) ~~the authors~~ estimated the performance and power curve of a ground-generation, ~~rigid~~ fixed-wing AWES by generating power-optimal trajectories and validate~~e~~ing them against Ampyx AP2 data (Licitra, 2018; Malz et al., 2019; Ampyx, 2020). The optimal, single-loop trajector~~ies are~~y was defined by a simple power law approximation of the wind speed profile. Because of the the up-scaling drawbacks of single-kite AWES, De Schutter et al. (2019) analyze~~s~~d the performance of utility-scale, stacked multi-kite systems, using the same optimization framework as this research. Two logarithmic wind speed profiles, one onshore and one offshore, provided boundary conditions

for the non-linear optimization problem. ~~Aull et al.~~Aull et al. (2020) explored the design and sizeing of fly-gen rigid wing AWES based on a steady-state model with simple aerodynamic and mass-scaling approximations. The wind resource ~~is~~ was described by an exponential wind shear model with Weibull distribution. An alternative approach to estimating AWES energy production using the Dutch Offshore Wind Atlas (DOWA), light detection and ranging (LiDAR) and ERA5 global reanalysis wind data set can be found in (Schelbergen et al., 2020). The authors used principal component analysis and k-means clustering to determine representative wind speed profiles for a part of the Netherlands and the North Sea. They derived power curves and estimated AEP from wind statistics for several locations.

AWES need to dynamically adapt their flight trajectory to changing winds in order to optimize power production. Wind velocity profiles are governed by environmental, location-dependent conditions (e.g. surface roughness) and weather phenomena on a multitude of temporal and spatial scales, subject to diurnal and seasonal patterns. The preferable means of determining wind conditions are long-term, high resolution measurements, which at mid-altitudes can solely be achieved by long-range ~~light detection and ranging~~ LiDAR. Numerical mesoscale weather prediction models such as the weather research and forecasting model (WRF), which is well known for conventional WT siting applications (Salvação and Guedes Soares, 2018; Dörenkämper et al., 2020), are used to estimate wind conditions on time scales of a few minutes to years. These numerical simulations should be corrected for systematic errors using measurements from LiDAR during site assessment and deployment as well as multi-year, long-term wind simulations. An investigation using simulated long-term wind statistics is beyond the scope of this paper. Measuring wind conditions at mid-altitudes is costly and difficult, due to reduced data availability (Sommerfeld et al., 2019a). Additionally, measurements are hard to find, because they are typically proprietary. Therefore, wind data in this study are exclusively based on uncorrected WRF mesoscale simulations (Skamarock et al., 2008). The same trajectory optimization methodology can be applied to any wind data, but is here illustrated with WRF data. We compare conventional WT hub-height based power curves to optimal AWES performance for an onshore location in northern Germany near the city of Pritzwalk (Sommerfeld et al., 2019b) and an offshore location at the FINO3 research platform in the North Sea.

The key contribution of this paper is the derivation and analysis of optimal AWES performance, operating height, trajectory, power and AEP, based on a dynamic optimization model, subject to realistic wind profiles. Another goal is to illustrate the problem of describing AWES power curves and estimating ~~annual energy prediction~~ AEP, because ~~no to agreed upon standard wind conditions or reference height exist.~~ AWES continuously change their operating heights and standard wind conditions have not yet been defined. The AWES glossary defined reference height as the pattern trajectory height, which is the time-averaged height during thee power production (reel-out) phase (Airborne Wind Europe, 2021). ~~We~~ This research compares the impact of different reference heights on the power curve and AEP ~~and propose a proxy for AWES operating height as a proxy~~. This is achieved by clustering the simulated wind velocity vectors using k-means clustering. We investigate the impact of number of clusters on AEP as the choice of wind conditions impacts the performance of any wind energy converter. Optimizing the AWES trajectories only for a representative subset of profiles reduces the computational cost significantly, while maintaining important wind profile characteristics. Results from the `awebox` optimization framework are compared to a quasi steady-state reference model (QSM). ~~impact of wind data is visualized by comparing results based on optimized trajectories to a quasi steady-state AWES model.~~

~~In summary, this manuscript provides insight into typical onshore and offshore wind conditions up to 1000 m, their variation and the potential application of clustering to identify representative wind speed profiles and in turn yield more realistic AWES power and energy estimation. Firstly, the wind resource and its underlying wind model are described. The model data is then categorized into several clusters and selected wind profiles are implemented into an optimization framework to determine power-optimal trajectories. Results are then referenced against a quasi steady-state AWES model, subject to the same wind profiles.~~

The paper is structured as follows. Section 2 introduces the mesoscale WRF model set-up and compares the onshore and offshore wind resource. Section 3 introduces the k-means clustering algorithm and summarizes results of clustered wind velocity profiles (both longitudinal and lateral wind components) for 10 representative clusters. These include cluster-averaged profiles and correlation with seasonal, diurnal and atmospheric stability. Section 4 introduces the dynamic AWES model, comprising of aircraft, tether and ground-station models. Section ~~5.1~~ 5 ~~introduces~~ describes the `awebox` optimization framework. It summarizes aircraft, ~~tether and ground station models as well as~~ system constraints and initial conditions ~~initialization~~ used to produce the results shown in Section 6. These include flight paths and time series of various performance parameters, and a statistical analysis of tether length and operating altitude. Furthermore, we compare power curve ~~characterization, capacity factor~~ and AEP estimates. Based on these results, an AWES power coefficient is defined to approximate AWES efficiency and power based on system size and wind speed. Finally, Section 7 concludes with an outlook and motivation for future work.

2 Wind conditions

This study compares ~~the general~~ ground-generation AWES performance and power curves at ~~a~~ representative onshore and offshore locations in Europe (~~fig~~ Figure 1). Wind conditions for the chosen years are assumed to be representative of ~~that~~ these locations. The comparison and implementation of long-term data from wind atlases is beyond the scope of this research. The onshore wind data is for ~~at~~ the Pritzwalk Sommersberg airport (lat: $53°10'47.00''$N, lon: $12°11'20.98''$E) in northern Germany and comprises 12 months of WRF simulation data between September 2015 and September 2016. The area surrounding the airport mostly consists of flat agricultural land with the town of Pritzwalk to the south and is therefore a fitting location for wind energy generation ~~(see~~ Sommerfeld et al. (2019a) and Sommerfeld et al. (2019b) for details~~)~~. The FINO3 research platform in the North Sea (lat: $55°11,7'$N, lon: $7°9,5'$ E) was chosen as a representative offshore location due to the proximity to several offshore wind farms and the amount of comprehensive reference measurements (Peña et al., 2015). The offshore simulation covers the time frame between September 2013 and September 2014.

2.1 Mesoscale model

The mesoscale simulations in this study were carried out using the weather research and forecasting (WRF) model ~~from~~. The onshore simulation was performed with version 3.6.1 (Skamarock et al., 2008) ~~before~~ prior to the 2018 release of WRF version 4.0.2 (Skamarock et al., 2021) in which the offshore simulations were computed. The setup of the model has been adapted and constantly optimized for wind energy applications by the authors of the present manuscript with the framework of various

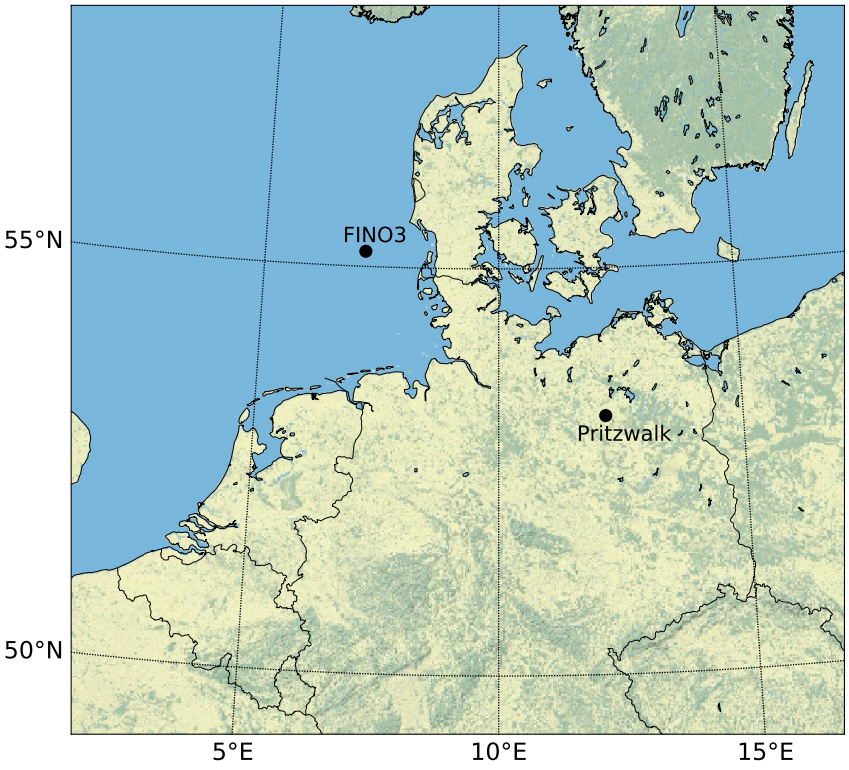

Figure 1. Map of northern Germany with the representative onshore (Pritzwalk) and offshore (FINO3) locations highlighted by black dots.

projects and applications in recent years (Dörenkämper et al., 2015, 2017; Dörenkämper et al., 2020; Hahmann et al., 2020; Sommerfeld et al., 2019b).

The focus of this study is not on the detailed comparison between mesoscale models, but on AWES performance subject to representative onshore and offshore wind conditions determined based on clustered wind profiles (described in Section 3). Both WRF models provide adequate wind data for for the assessment of AWES performance, even though the setup and time frame are different.

~~Both~~ Each of the simulations consists of three nested domains ~~centered~~ around the respective locations of interest shown in Figure 1 ~~either the FINO3 met mast (Figure 1) or the Pritzwalk Sommersberg airport.~~ Atmospheric boundary conditions are defined by ERA-Interim (Dee et al., 2011) for the onshore location and by ERA5 (Hersbach and Dick, 2016) reanalysis data for the offshore location, while sea surface parameters for the offshore location are based on OSTIA (Donlon et al., 2012). These data sets have proven to provide good results for wind energy relevant heights and sites (Olauson, 2018; Hahmann

et al., 2020). Both simulations use the MYNN 2.5 level scheme for the planetary boundary layer (PBL) physics (Nakanishi and Niino, 2009). While the onshore simulation was performed in ~~one~~ a single 12 month spanning simulation~~s~~ (~~01.09.2015 - 31.08.2016~~ 2015-09-01 to 2016-08-31), the offshore simulation period consisted of 410 days (~~30.08.2013 - 14.10.2014~~ 2013-08-30 to 2014-10-14) that ~~were~~ was split into 41 simulations of 10 days each with an additional 24 hours of spin-up time per run. Spin-up describes the period during which the model produces unreliable results due to the initialization based on a coarser, global atmospheric reanalysis data set. The data from the mesoscale models sigma levels (terrain-following) ~~were~~ are transformed to the geometric heights using the post-processing methodology described in Dörenkämper et al. (2020). Table 1 summarizes the key parameters of the model settings used in this study. All simulations were run on the *EDDY* High-Performance Computing clusters at the University of Oldenburg (Carl von Ossietzky Universität Oldenburg, 2018).

Table 1. Key setup parameters of the onshore and offshore mesoscale model simulations using the WRF model by Skamarock et al. (2008)

Model Parameter	Settings	
	Onshore	Offshore
WRF model version	3.5.1	4.0.2
time period	~~01.09.2015 - 31.08.2016~~ 2015-09-01 to 2016-08-31	~~30.08.2013 - 14.10.2014~~ 2013-08-30 to 2014-10-14
Reanalysis	ERA-Interim	ERA5 & OSTIA
Horizontal grid size (D01, D02, D03)	120~~x~~ ×120, 121~~x~~ ×121, 121~~x~~ ×121	150~~x~~ ×150, 151~~x~~ ×151 , 151~~x~~ ×151
Resolution (D01, D02, D03)	27 km, 9 km, 3 km	18 km, 6 km, 2 km
Vertical levels	60 sigma levels (about 25 below 2 km)	60 sigma levels (about 25 below 2 km)
Nesting	1-way	1-way
Initialisation strategy	single run	240 h runs plus 24 h spinup time
Nudging	Analysis nudging (FDDA)	Analysis nudging (FDDA)
PBL scheme	MYNN level 2.5 scheme	MYNN level 2.5 scheme
Micro physics	Ferrier scheme	WRF Single–moment 5–class scheme
Long wave & shortwave radiation	RRTM & Dudhia	RRTMG scheme

2.2 Wind regime

Figure 2 depicts the wind roses of the annual wind conditions at 100 (top) and 500 m (bottom) height onshore (left) and offshore (right). The dominant wind direction at both locations is southwest, turning clockwise with increasing altitude.

Directional variability decreases and wind speed increases with height, following the expected trends in the northern hemisphere (Arya and Holton, 2001; Stull, 1988). The average onshore wind direction turns about 14° between 100 and 500 m, whereas average offshore wind direction only veers approximately 5°. The offshore wind direction turns approximately 10° additional degrees above 500 m, resulting in roughly the same westerly wind direction at high altitudes at around 1000 m. Due to prevailing unstable conditions offshore, a strong mixing with height is found resulting in less veer across the heights investigated in this study. The wind shear at the offshore location is lower compared to the onshore location due to lower surface roughness.

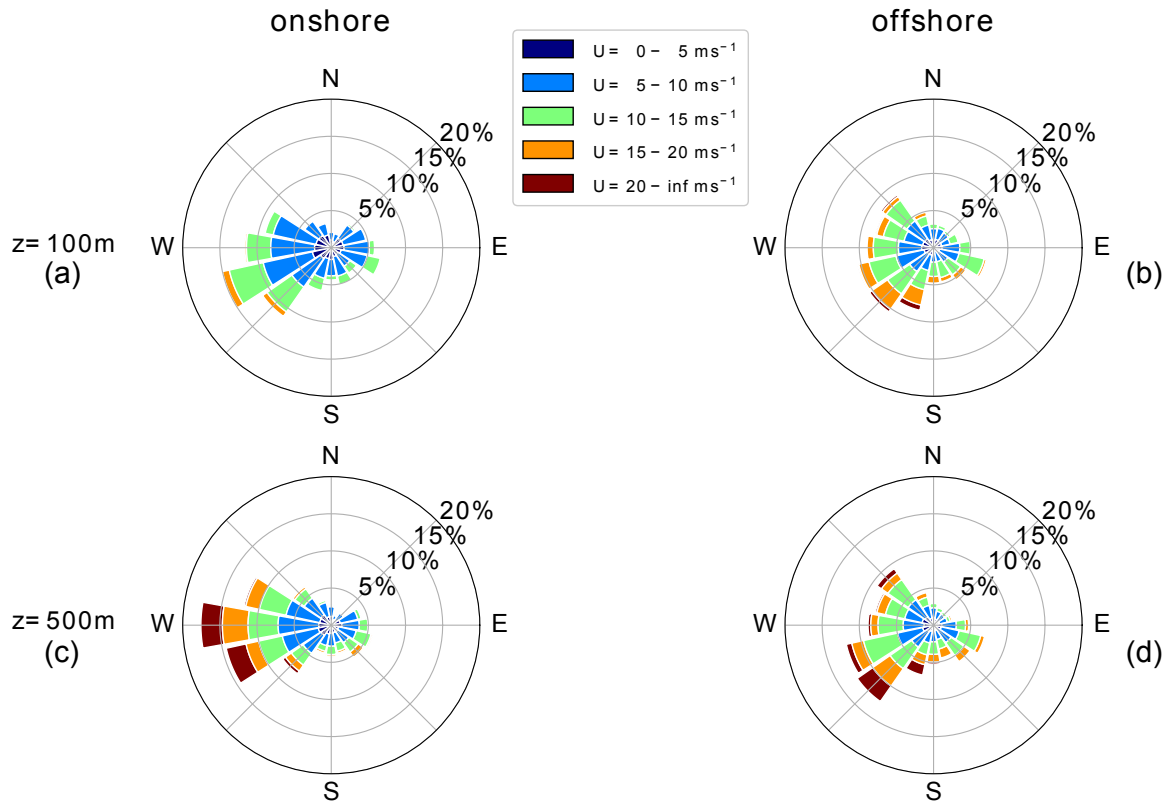

Figure 2. Wind roses of annual wind direction and speed statistics at Pritzwalk (onshore) and FINO3 (offshore) ~~presented as wind roses~~ for 100 and 500 m.

Figure 3 shows the annual horizontal wind speed probability distributions at each ~~individual~~ height level for both locations. These distributions give an insight into the wind speed statistics at ~~individual~~ specific heights, but not into the statistics of the wind profile shapes, which are important for AWES power and trajectory optimization. The chosen nonlinear color~~range~~ gradient allows for the representation of the entire relative probability range. Onshore (left) wind speeds are relatively low and have a fairly narrow ~~range~~ deviation below 300 m, due to dominant surface effects. Above this height the distribution broadens, but a high probability of low wind speeds remains for the full height range. The distributions show bi-modal characteristics caused by different atmospheric stratification. Low wind speeds are commonly associated with unstable and high wind speeds with neutral or stable atmospheric conditions.

Such multimodal distributions at higher altitudes are better described by the sum of two or more probability distributions, as standard Weibull or Rayleigh distributions can not capture this phenomenon (Sommerfeld et al., 2019a). Offshore (right) wind speeds on the other hand have a wider distribution at all heights as they are less ~~inhibited~~ affected by surface effects. Similar to onshore, the offshore frequency distribution also shows a high probability of lower wind speeds (between 5-10 ms^{-1}) at all heights. Higher wind speeds at lower altitudes benefits conventional WT and weakens the argument for offshore AWES as

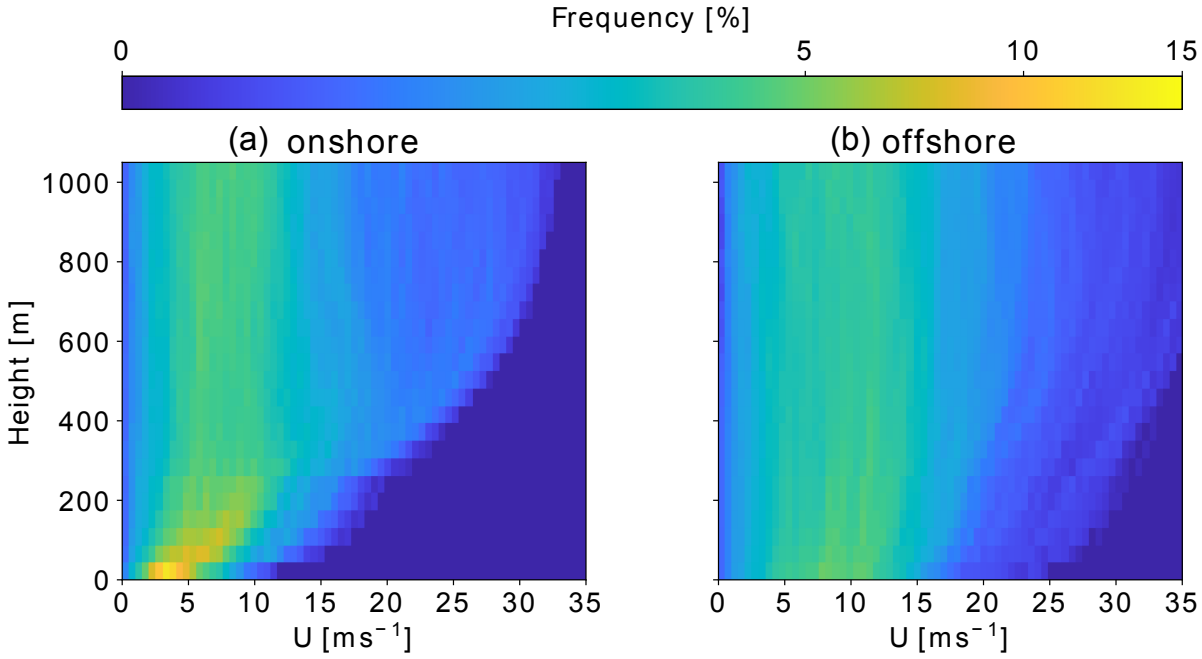

Figure 3. Comparison of WRF-simulated annual wind speed probability distribution at each height level between Pritzwalk (onshore left) and FINO3 (offshore right) up to 1000 m. A nonlinear color scheme was chosen to represent the high probability of low altitude onshore winds while still differentiating the lower, wide spread frequencies at higher altitudes.

one of their benefits would be to harness energy from the stronger winds at higher altitudes. ~~Nevertheless, also AWES benefit from these higher wind speeds.~~ Additional reasons for placing AWES offshore are safety and land use regulations and potential cost benefits of a smaller support structure (offshorewind.biz, 2018; Lunney et al., 2017; Ellis and Ferraro, 2016). If AWES can reliably operate autonomously they might still provide a cheaper source of electricity than conventional WT, due to their reduced material cost.

Atmospheric stability of the boundary layer, which highly affects the wind speed profile shape, is commonly characterized using the Obukhov length $\mathcal{L}$ (Obukhov, 1971; Sempreviva and Gryning, 1996). Here the application is extended to mid-altitudes. $\mathcal{L}$ is defined by the simulated friction velocity u_*, virtual potential temperature θ_v, potential temperature θ, kinematic virtual sensible surface heat flux Q_S, kinematic virtual latent heat flux Q_L, the von Kármán constant k and gravitational acceleration g:

$$\mathcal{L} = \left(\frac{-u_*^3 \theta_\mathrm{v}}{kg}\right)\left(\frac{1}{Q_\mathrm{S}} + \frac{0.61}{Q_\mathrm{L}\theta}\right). \quad (1)$$

Various stability classifications using Obukhov length are defined for different wind energy sites. Table 2 summarizes the Obukhov length bin widths (Floors et al., 2011) and the frequency of occurrence of each stability class onshore and offshore, consistent with Sommerfeld et al. (2019b).

Neutral stratification occurs approximately 20% of the year at both locations. The lower heat capacity of the land surface leads to a faster heat transfer and a quicker surface cool-off which favors the development of stable stratification (≈17% onshore vs ≈6% offshore). The offshore location has a higher probability of unstable conditions which is likely caused by a warmer ocean surface compared to the air above (Archer et al., 2016).

Table 2. Stability classes based on Obukhov lengths (Floors et al., 2011) and associated annual probability at Pritzwalk (onshore; 01.09.2015 - 31.08.2016) and FINO3 (offshore; 30.08.2013 - 14.10.2014), based on WRF results.

Stability class	$\mathcal{L}$ [m]	onshore	offshore
Unstable (U)	$-200 \leq \mathcal{L} \leq -100$	7.27%	13.66%
Nearly unstable (NU)	$-500 \leq \mathcal{L} \leq -200$	7.09%	16.34%
Neutral (N)	$\lvert\mathcal{L}\rvert \geq 500$	20.71%	22.82%
Nearly stable (NS)	$200 \leq \mathcal{L} \leq 500$	12.56%	5.15%
Stable (S)	$50 \leq \mathcal{L} \leq 200$	17.24%	6.20%
Very stable (VS)	$10 \leq \mathcal{L} \leq 50$	10.04%	2.96%
Other	$-100 \leq \mathcal{L} \leq 10$	25.09%	32.87%

Both unstable and stable conditions can lead to non-logarithmic and non-monotonic wind speed profiles. Unstable conditions are often accompanied by almost uniform wind speed profiles due to increased mixing, whereas low level jets (LLJs) can develop during the nocturnal stable onshore boundary layer (Banta, 2008). Both locations have a high chance of unassigned ~~"Other"~~ conditions (labeled as "Other") which are mostly associated with low wind speeds.

3 Clustering of wind conditions

~~The power output of AWES highly depends on the wind velocity and its variation with height. Many temporal and spatial averages, correlations and approximations are used to describe the constantly varying wind conditions and their affect on wind energy converters. Instead of reverting to simple approximations such as the logarithmic wind speed profile, representative, WRF-simulated wind velocity profiles are chosen to compare AWES performance as realistically as possible.~~

WRF-simulated wind velocity profiles are chosen to compare realistic AWES performance. Onshore (Pritzwalk) and offshore (FINO3) data are classified into groups to determine representative profiles. An accepted methodology to describe the near-surface atmosphere is atmospheric stability, commonly quantified by the Obukhov length (Obukhov, 1971; Sempreviva and Gryning, 1996) which exclusively uses surface data (Section 2.2 and Equation (1)). Previous studies (Sommerfeld et al., 2019a, b) showed that Obukhov-length-classified wind speed profiles diverge with height, especially during neutral and stable conditions, which indicates vertically heterogeneous atmospheric stability and suggests that surface-based stability categorization is insufficient for higher altitudes. Clustering wind velocity profiles based on their similarity ~~was shown~~ results in more cohesive profile groups (Schelbergen et al., 2020) ~~(Figures A1 and A2)~~. In contrast to classifying the wind regime by atmo-

spheric stability, which requires temperature and heat flux data, clustering only uses wind data at multiple heights and groups profiles by similarity. Therefore, clustering can also be applied to wind-only measurements such as LiDAR.

The k-means clustering algorithm (Pedregosa et al., 2011) used in this study was chosen for its ease of use and scalability, due to the high dimensionality of the data set. Many other algorithms produce similar results, but a comparison between clustering algorithms is beyond the scope of this research.

Before clustering, the two horizontal wind velocity components u and v, whose vertical variation define the wind velocity profile, are rotated such that the main wind component (average wind direction up to 500 m) u_{main} points in the positive x-direction and the ~~deviation~~ transverse component $u_{\text{deviation}}$ is perpendicular to it, pointing in the positive y direction. This removes the directional dependency of the wind velocity profiles and results in more homogeneous clusters and simplifies the comparison of wind data and `awebox` results. It is analogous to assuming omnidirectional operation. The AWES still needs to adjust to changes in wind conditions with height.

The algorithm assigns each data point, in our case wind velocity profile up to 1000 m, which comprises approximately 30 heights and 2 directions, to one of k clusters represented by their respective cluster mean (also referred to as centroid). These centroids are ~~arranged~~ chosen such that they minimize the sum of the Euclidean distances to every data point within each cluster. ~~, also referred to as "inertia" or "within-cluster sum-of-squares", i.e. the cost function of the algorithm~~ This cost function is also reffered to as "inertia" or "within-cluster sum-of-squares". As such, the centroids are usually not actual data points, but rather the average of that cluster, and will at best coincide with a data point by chance. The resulting cluster label ~~number~~ is the result of random initialization and does not have any mathematical meaning. Therefore, the clusters are sorted cluster by average wind speed up to 500 m for the following analyses. The variable k refers to the fixed, predefined number of clusters. The choice of k significantly affects the accuracy of the wind resource description, the resulting power and AEP predictions (Section 6.4) as well as the computational cost associated with clustering (pre-processing) and AWES trajectory optimization (processing). The choice of k is informed by the elbow method, named after the characteristic line chart which resembles an arm, and silhouette score. The "elbow" (the point of inflection on the curve) is a good indication that the underlying model fits well for the corresponding number of clusters and k is chosen at a point where the inertia reduction becomes marginally small or decreases linearly (Pedregosa et al., 2011). ~~The elbow method and silhouette score (Figure 4 (c)) indicate preferable choices of k. The elbow method (Sub-Figure a in Figure 4) compares the inertia trends as a function of k. The parameter k is often chosen at a point where the inertia reduction becomes marginally small or decreases in a linear fashion with increasing number of clusters, often represented by a sharp bend or elbow in the inertia trend. A k of 20 seems to be a decent choice for the available data sets as inertia only decreases moderately for higher number of clusters which does not justify the additional computational cost.~~ Absolute values of inertia are not a normalized metric and therefore scales with size of the considered data set. The silhouette coefficients on the other hand are normalized between -1 (worst) and 1 (best).~~and~~ They indicate the membership of a data point to its cluster in comparison to other clusters, i.e. proximity of each data point in one cluster to data points in neighboring clusters (Pedregosa et al., 2011). A negative value suggests that a data point is assigned to the wrong cluster. The silhouette score ~~(c Figure 4)~~ is the average of all silhouette coefficients for a fixed number of clusters k.

~~Onshore (b) and offshore (d) silhouette coefficients for a representative k of 10. Each cluster is sorted by average wind speed up to 500 m and colored corresponding to the cluster centroids shown in Figure 5. Silhouette coefficients (b,d) and the resulting silhouette score (c) indicate good cluster coherence at both locations. The impact of number of clusters on AEP is later discussed in Sub-section 6.4.~~

Figure 4 (a) shows the inertia (within-cluster sum-of-squares) for both locations. Figures 4 (b) and 4 (d) show the silhouette coefficients for $k = 10$, which is chosen here for visualization purposes. The corresponding average silhouette score is depicted by a dashed, red, vertical line. Each cluster is sorted by average wind speed up to 500 m and colored corresponding to the cluster centroids shown in Figure 5. Performing this silhouette score analysis for multiple k results in the trend shown in Figure 4 (c). A k of 20 seems to be a decent choice for the available data sets as inertia only decreases moderately for higher number of clusters which does not justify the additional computational cost. Similarly, the silhouette score remains almost constant for higher numbers of clusters. Therefore $k = 20$ has been chosen for later analyses in Section 6.

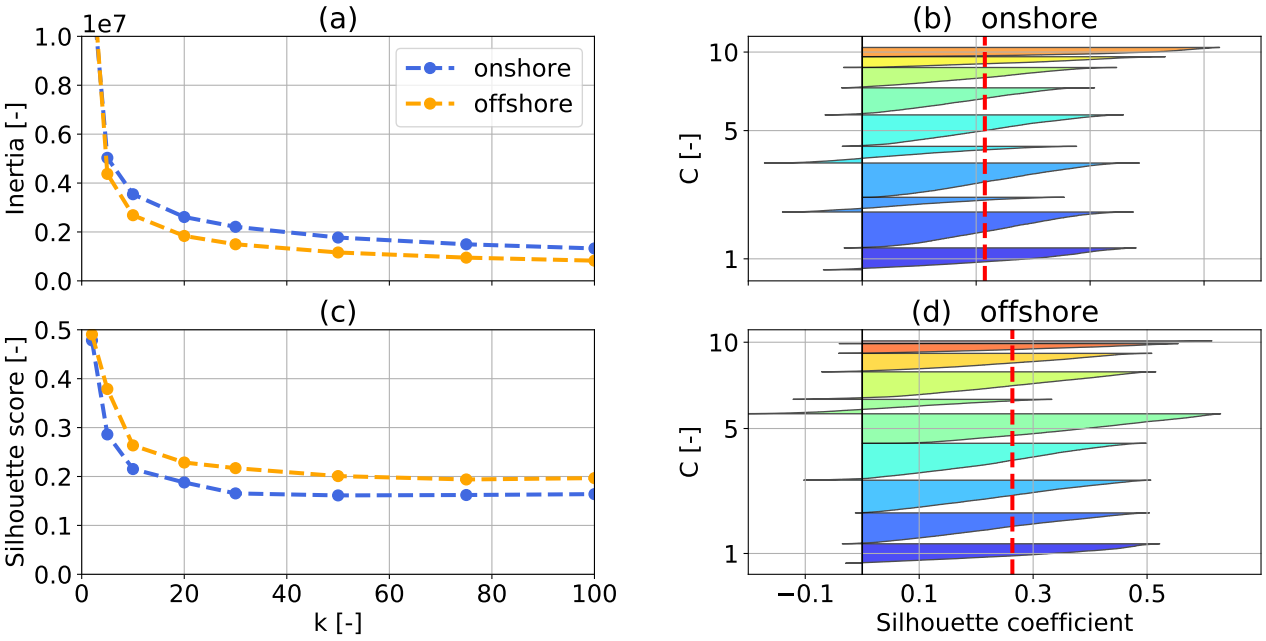

Figure 4. k-means clustering inertia over ~~number~~ of cluster k (a) for one year of onshore (blue) and offshore (orange) wind velocity profiles up to 1000 m. Silhouette score (c), average silhouette coefficients, over number number of cluster k for both locations. Onshore (b) and offshore (d) silhouette coefficients (k=10, number of clusters chosen for presentation purposes) express the distance to neighbouring clusters. The red dashed line represents the silhouette score.

3.1 Analysis of clustered profiles

For visualization purposes, the following sub-sections describe the wind conditions at both locations using only k=10 clusters~~,~~ ~~instead of the k=20 clusters chosen to analyze AWES performance in Section 6~~. ~~Sub-Figures a and b in~~ Figures 5 (a) and 5 (b) show~~s~~ the average ~~wind speed~~ profiles of the clustered wind velocity profiles, also referred to as centroids. The magnitude of the WRF-simulated wind velocity profiles that define their respective cluster are depicted in grey. Within a cluster, the wind speed profiles span a fairly narrow range of wind speeds except for a few outliers (Figures A1, A2) **Roland: Why do we now jump to the appendix? Markus: I moved these figures to the appendix, because the paper already has a lot of figures. I believe these figures add some supplementary information, but are not necessary.** , indicating coherent clusters. Clusters are sorted by average centroid speed up to 500 m, represented by their colors and labels ($C = 1 - 10$).

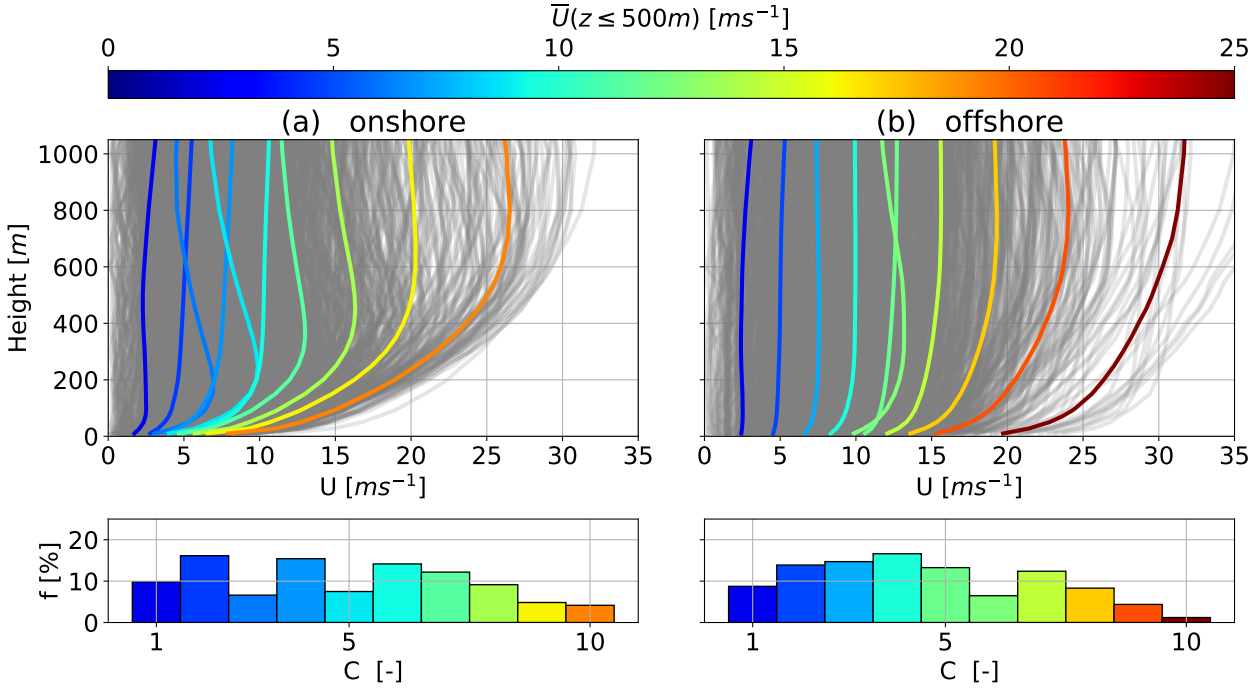

Figure 5. Onshore (left) and offshore (right) average annual wind speed profiles (~~or~~centroids) resulting from ~~the~~ k-means clustering ~~process~~ for k = 10 ~~over height~~ (top). Comprising WRF simulated wind velocity profiles depicted in grey. Centroids are sorted, labeled and colored in ascending order of average wind speed up to 500 m. The corresponding cluster frequency f for each cluster C is shown below.

As expected offshore (Figure 5 right) low altitude wind speeds are higher and wind shear is lower than onshore (addFigure 5 left). Overall, offshore centroids are wider spread in comparison to the onshore profiles. The associated annual centroid frequency of occurrence for k=10 is shown below in Figure 5. Wind speeds of the first and sixth offshore centroid decrease at higher altitude which could be caused by local or large-scale weather phenomenon. Both these clusters have a comparatively low probability. The first three onshore and offshore clusters exhibit very low wind shear with almost constant wind speed

above 200 m. Onshore cluster 5, which seems to comprise of non-monotonic profiles as its centroid has a distinct LLJ nose at about 200 m, occurs about 5% of the time. Onshore centroids of clusters 7 and 8 also show a slight wind shear inversion at higher altitudes.

Evidently, the wind speed magnitude plays a dominant role in clustering as the resulting centroids are nearly ordered in terms of speed, especially offshore. This can lead to profiles whose shape significantly differs from the one of the centroid to be assigned to a cluster due to similar average wind speed. A clearer wind profile shape distinction could be achieved by normalizing the data before clustering it (Molina-García et al., 2019; Schelbergen et al., 2020). Normalization was ~~deferred~~was not applied in this study to simplify and clarify the clustering procedure as the focus of this manuscript is on the derivation and comparison of ~~AWES~~ power curves. With this application in mind, it is important to note that low speed profiles with an almost constant speed up to high altitudes add up to about 20-30 % of annual probability. This fact is often averaged out when only long term average wind speed profile shapes are considered and can lead to an overestimation of wind speeds at higher altitudes. AWES therefore need to be able to either operate under such low speed conditions or be able to safely land and take-off.

3.2 Analysis of clustered statistics

Figures 6 to 8 summarize the correlation between ~~representative~~ clusters ~~(k=10)~~ and monthly, diurnal and atmospheric stability for the onshore (top row) and offshore (bottom row) location. This reveals patterns within the data set and gives insight into the wind prevailing regime. Here only $k = 10$ clusters are chosen for presentation purposes, even though we previously determined $k = 20$ to be a good choice for the wind data set.

Clusters are sorted in ascending order of centroid average wind speed up to 500 m and colored accordingly. The corresponding centroids are shown in Figure 5.

Both locations follow a distinct annual pattern (Figure 6) during which profiles associated with high wind speeds increase during the winter months and profiles with low wind speeds are predominantly found in summer. The two onshore and offshore clusters associated with the highest wind speed are almost exclusively present during November to February.

Offshore data shows almost no diurnal variability (Figure 7) with only a slight increase of clusters associated with lower wind speeds during daytime. Onshore clusters on the other hand are more dependent on the diurnal cycle with a higher likelihood of low speed clusters after sunrise. The frequency of onshore cluster 5, which comprises a LLJ nose (Figure 5), drops to almost zero during daytime and increases during nighttime, substantiating the assumption that this cluster is associated with nocturnal LLJs.

The clustered wind velocity profiles and their associated speed and shape correlate with atmospheric stability as expected (Figure 8). Low wind speed clusters make up about 20% to 30% of the annual wind resource. These clusters exhibit Obukhov lengths close to zero (likely caused by very low friction velocity u_*) and are classified as "other" because they do not fall within one of the other atmospheric stability classes according to (Floors et al., 2011) (Table 2). Unstable (U) and near unstable (NU) conditions are associated slightly higher wind speeds than "other" at both locations. The highest wind speeds develop during neutral (N) and near stable (NS) conditions. It ~~should~~ needs to be acknowledged that strong winds driven by large

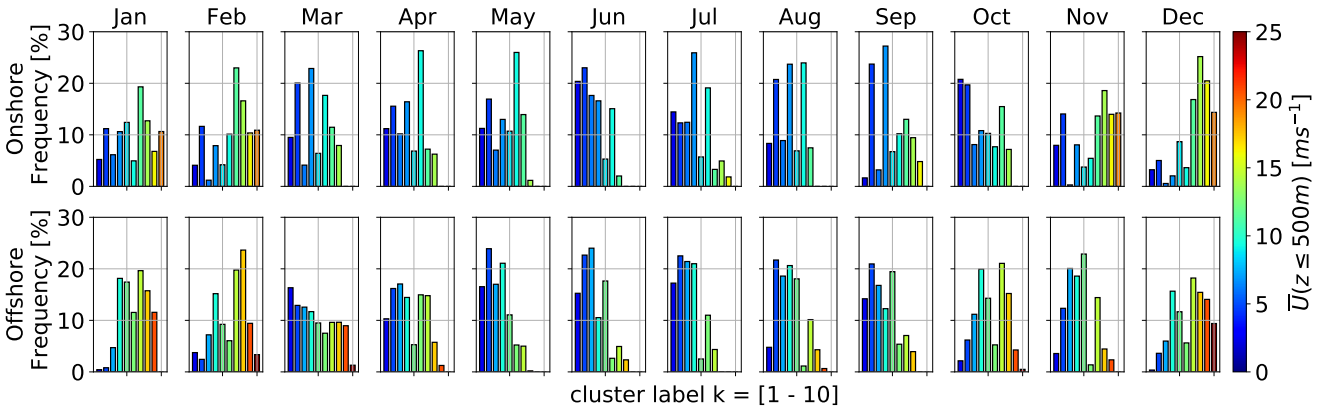

Figure 6. Monthly frequency of k-means clustered onshore (top) and (offshore) wind velocity profiles for a representative k=10. Clusters are sorted and colored by average wind speed up to 500 m. Centroids associated with each cluster can be found in Figure 5.

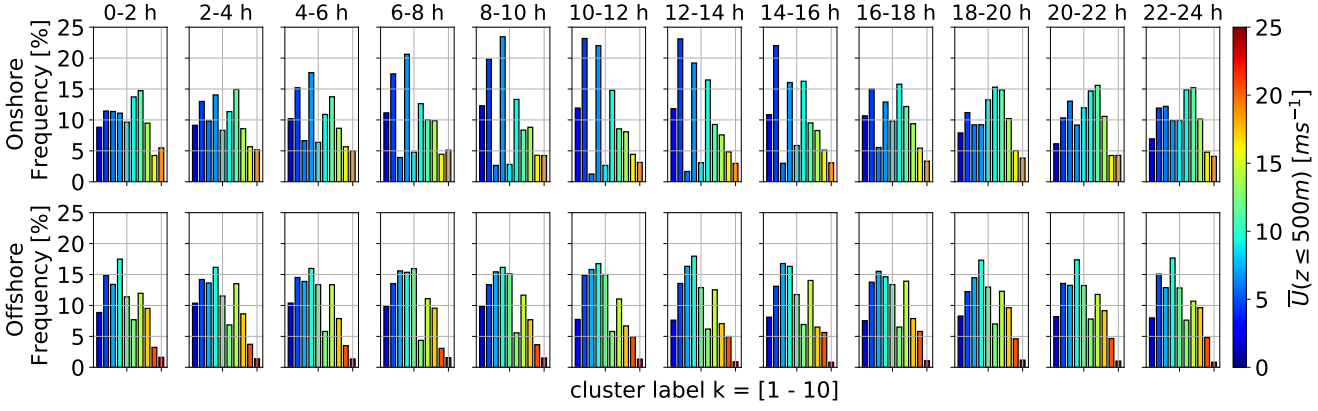

Figure 7. Diurnal frequency of k-means clustered onshore (top) and (offshore) wind velocity profiles for a representative k=10. Clusters are sorted and colored by average wind speed up to 500 m. Centroids associated with each cluster can be found in Figure 5.

pressure gradients tend to drive the stratification towards neutral. LLJ profiles associated with onshore cluster 5 are most likely to develop during stable (S) and very stable (VS) conditions.

In conclusion, k-means clustering is able to capture and reveal temporal variations in the wind regime as well as location specific wind profile shapes up to high altitudes. Wind speed magnitude seems to determine the resulting clusters more than profile shape. Nonetheless, less common, non-monotonic profile shapes, for example profiles with LLJs, ~~were~~ can be identified. Normalizing the profiles before clustering will give more insight into the different vertical profile shapes, but was not pursued in the present study. The corresponding cluster frequency follows the expected temporal trend and atmospheric stability association.

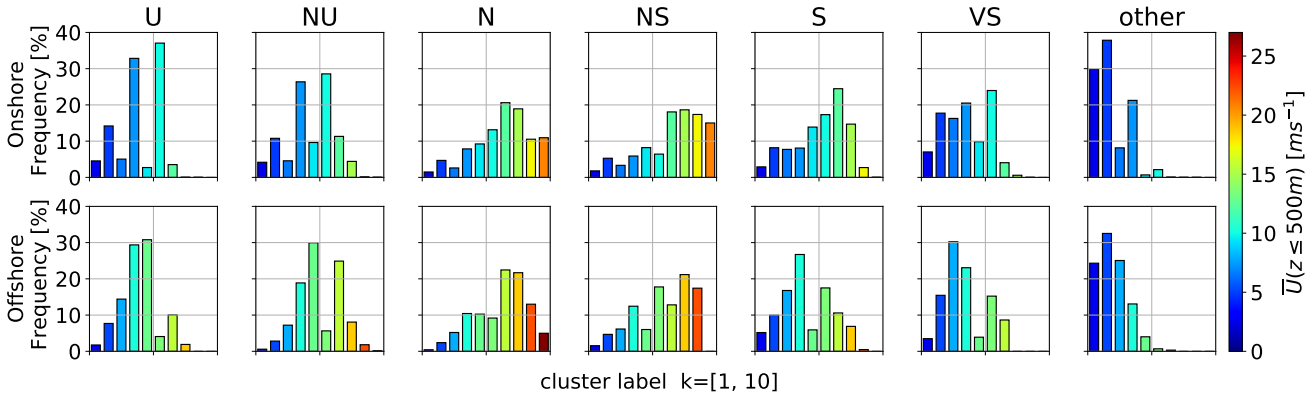

Figure 8. Atmospheric stability (U: unstable, NU: nearly unstable, N: neutral, NS: nearly stable, S: stable, VS: very stable) distribution of k-means clustered onshore (top) and (offshore) wind velocity profiles for a representative $k = 10$. The associated stablility classes are based on Obukhov length (Table 2). Clusters are sorted and colored by average wind speed up to 500 m. Centroids associated with each cluster can be found in Figure 5.

4 Dynamic AWES model

This section introduces the dynamic AWES models used in the `awebox` trajectory optimization framework (De Schutter et al., 2020) (Section 5.1). Firstly, Sub-section 4.1 gives an overview of the AWES configuration. The following sub-sections introduce the aerodynamic model (Sub-section 4.2), the aircraft mass model (Sub-section 4.3). The AWES model comprises of an aerodynamic model (Sub-section 4.2), an aircraft mass model (Sub-section 4.3), a rigid straight tether (Sub-section 4.1) and a ground station model (Sub-section 4.4).

4.1 AWES Model configuration

We consider a 6 degree of freedom (DOF) rigid-wing aircraft model which is connected to the ground via a rigid straight tether. thereby reducing By introducing the tether, the DOF is reduced to 5, a minimized set of generalized coordinates. It uses precomputed quadratic approximations of the aerodynamic coefficients which are controlled via aileron, elevator and rudder deflection rates (Malz et al., 2019). The longitudinal motion of the tether is controlled by the tether jerk $\dddot{l}_{tether}$ from which tether acceleration $\ddot{l}_{tether}$, speed $\dot{l}_{tether} = v_{\text{tether}}$ and length (l_{tether}) l are integrated determined by integration. The tether is modeled as a single solid rod which can not be subjected to support compressive forces (De Schutter et al., 2019). The rod is divided into $n_{aero} = 10$ elements segments and tether drag is calculated individually for each element relative to segment, using the local apparent wind speed (Bronnenmeyer, 2018)., with a tether drag coefficient of $c_{\text{D}}^{\text{tether}} = 1.$ The tether drag of every tether elements segment is equally divided between the two endpoints and finally transferred propagated to either the aircraft or ground station. This leads to an underestimation of total tether drag at the aircraft. Please refer to (Leuthold et al., 2018) for more details. The ground station itself is not explicitly modeled, but implemented as a set of constraints which play

a decisive role for the generated power of ground-generation AWES. Using a simplified model, optimal reel-out speed can be estimated from elevation ε and azimuth angle ϕ:

$$\dot{l}_{\text{out}} \approx \frac{1}{3} \cos\theta_{\varepsilon} \cos\phi \dot{l}_{\text{wind}}. \tag{2}$$

Therefore, reel-out speed is expected to remain below $10\ \text{ms}^{-1}$ as the wind speed hardly exceeds $20\ \text{ms}^{-1}$. A reel-in speed of $\dot{l}_{\text{in}} = 15\ \text{ms}^{-1}$ and reel-out speed of $\dot{l}_{\text{out}} = 10\ \text{ms}^{-1}$ are chosen, resulting in a reel-out to reel-in ratio of $\frac{2}{3}$ which is assumed to be within design limitations of the winch. A maximum tether acceleration of $\ddot{l} = 20\ \text{ms}^{-2}$ is imposed to comply with generator torque limits. The tether diameter is chosen such that rated power is achieved at $U_{\text{ref}} = 10\ \text{ms}^{-1}$. Tether force constraints enforce tension to remain positive whilst not exceeding the maximum tether stress, to which a safety factor of 3 is applied. This results in a tripling of the cross-sectional tether area. These ground station and tether constraints do not represent a fully optimized AWES, but rather a representative system.

4.2 Aerodynamic model

The presented model utilizes the Ampyx AP2 aerodynamic coefficients from De Schutter et al. (2020); Malz et al. (2019); Ampyx (2020). The AP2 reference is scaled to a wing area of $A = 20\ \text{m}^2$ while the aspect ratio is kept constant at $AR = 10$. The total drag coefficient $c_{\text{D,total}}$ of aircraft and tether highly depends on tether drag and therefore diameter d_{tether} and length l_{tether}, as well as the wing area A_{wing} and aerodynamic drag coefficient of the wing $c_{\text{D,wing}}$. We consider a straight, cylindrical tether with constant diameter and an aerodynamic tether drag coefficient $c_{\text{D,tether}}$ of 1.0, which would be even higher for braided tethers. Assuming a uniform wind, the line integral along the tether results in a total effective drag coefficient of:

$$c_{\text{D,total}} = c_{\text{D,wing}} + \frac{1}{4} \frac{d_{tether} l_{tether}}{A_{\text{wing}}} c_{\text{D,tether}} \tag{3}$$

See Houska and Diehl (2007); Argatov and Silvennoinen (2013) and van der Vlugt et al. (2019) for details.

Figure 9 depicts the effect of tether drag on the $A_{\text{wing}} = 20\text{m}^2$ scaled AP2 aircraft for tether lengths up to $l_{tether} = 1000\text{m}$. Lift Figure 9(a) and pitch moment Figure 9(c) are assumed to behave linearly, while changes in the drag coefficient Figure 9(b) are approximated by a quadratic function. Tether drag is independent of aircraft angle of attack and therefore added to the zero-lift drag coefficient c_{D0}. Glide ratio $c_L/c_{\text{D,total}}$ Figure 9(e) and ~~Loyd power factor~~ aerodynamic factor $c_{\text{R}}^3/c_{\text{D,total}}^2$ (Loyd, 1980) Figure 9(f) not only decrease significantly with tether length, but optimal values move towards higher angle of attack. This effect ~~with be~~ is less pronounced for larger wings ~~due to beneficial scaling effects~~ because the effect of tether drag reduces when scaling up to larger aircraft.

4.3 Aircraft mass model

The aircraft dynamics are described by a single ~~point mass~~ rigid body of mass m and moment of inertia J, with aerodynamic forces and moments applied to it. The dynamics of the tethered aircraft are highly dependent on aircraft mass m and moment

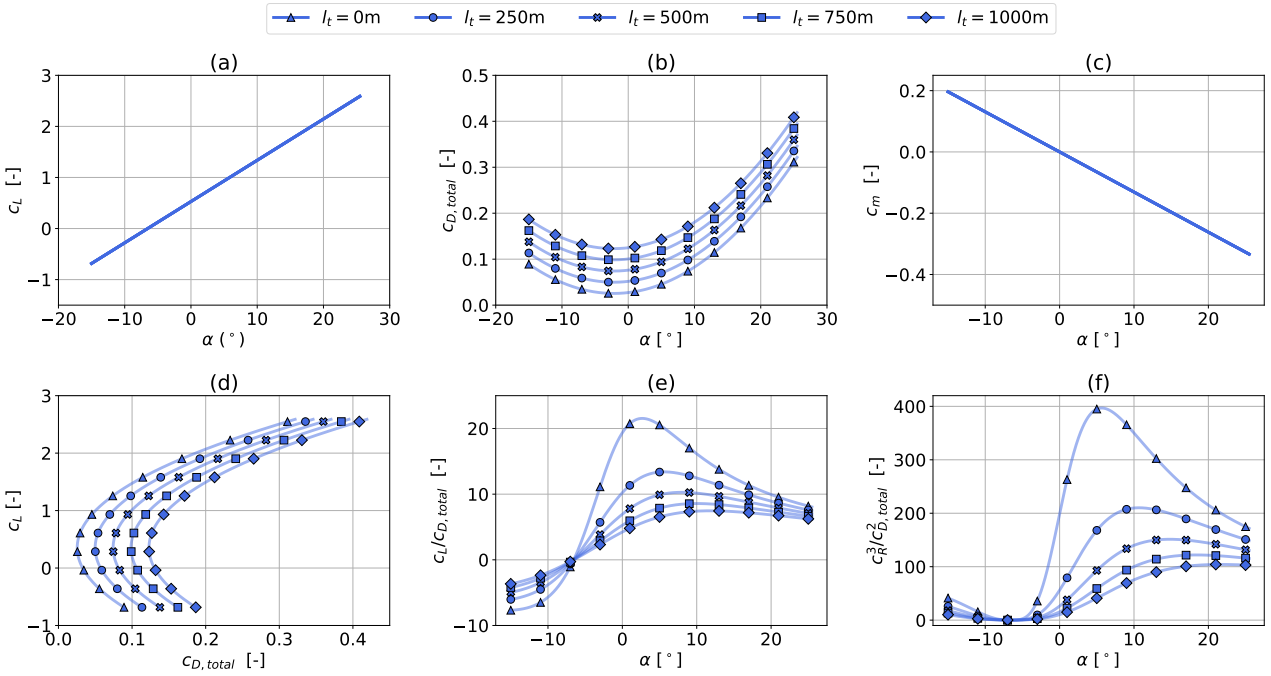

Figure 9. Ampyx AP2 reference wing aerodynamic lift c_{L} (a) and drag $c_{\mathrm{D,total}}$ coefficients (b) (Malz et al., 2019; Ampyx, 2020), including tether drag according to Equation (3), for a wing area A_{wing} of $20\mathrm{m}^2$ and tether diameter of $d_{tether} = 7.8\mathrm{mm}$ (Table 3. Tether length varies between 250 m and 1000 m. (c) shows the pitch moment coefficient c_{m} as a function of angle of attack. The bottom figures display lift over drag (d), lift-to-drag ratio over angle of attack (e) and $c_{\mathrm{R}}^3/c_{\mathrm{D,total}}^2$ over angle of attack. ~~according to Loyd~~ (Loyd, 1980).

of inertia J which are derived by upscaling the AP2 reference wing from $A_{\mathrm{wing}}^{\mathrm{AP2}} = 3\ \mathrm{m}^2$ to $A_{\mathrm{wing}} = 20\ \mathrm{m}^2$. Mass m_{scaled} and moment of inertia $\mathbf{J}_{\mathrm{scaled}}$ of a rigid wing aircraft scale relative to wing span b with a mass scaling exponent κ ~~(Equation (4)), based on Galileo's square–cube law.~~

$$m_{\mathrm{scaled}} = m_{\mathrm{ref}} \left(\frac{b}{b_{\mathrm{ref}}} \right)^{\kappa} \tag{4}$$

$$J\mathbf{J}_{\mathrm{scaled}} = J\mathbf{J}_{\mathrm{ref}} \left(\frac{b}{b_{\mathrm{ref}}} \right)^{\kappa+2} \tag{5}$$

Pure geometric scaling corresponds to Galileo's square-cube law decribed by $\kappa = 3$. ~~but~~ In reality, as has been seen for the development of conventional WTs, design and material improvements occur ~~with scaling~~ over time. A review of the available literature containing system mass details was conducted to identify an appropriate mass scaling factor. The results are shown in Figure 11~~;~~ depicting actual and anticipated AWES scale bounded by $\kappa = 2.2 - 2.6$ (grey area). We chose $\kappa = 2.4$ based on a curve fit of the available published sizing study data. This seems quite ambitions and might be achievable for soft wing AWES.

The mass of these hollow tensile structures filled with air mostly scales the wing surface, leading to significantly lower mass scaling exponents and more beneficial mass scaling. A parallel scaling study (Sommerfeld et al., 2020) investigates the impact of variable mass scaling exponents. ~~Based on a curve fit to the available published sizing study data, $\kappa = 2.4$ seems reasonable for future AWES development, but we leave a fulsome system AWES scaling study to future work. It can be assumed that lighter aircraft result in a lower cut-in wind speeds and higher power output.~~

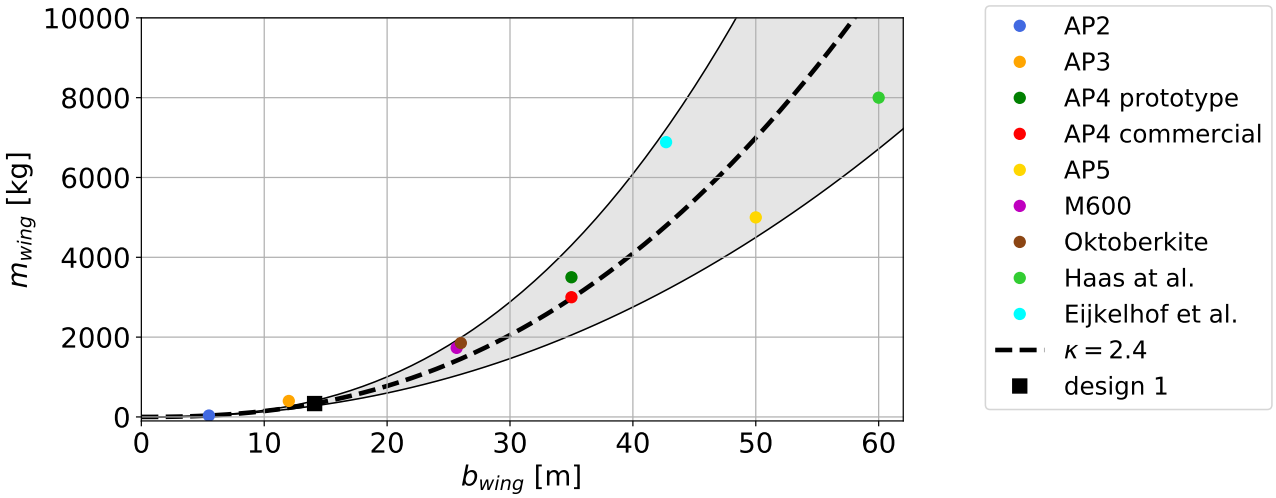

Figure 10. ~~Curve fit of published sizing study AWES aircraft mass~~ (Haas et al., 2019; Kruijff and Ruiterkamp, 2018; Eijkelhof et al., 2020; Ampyx, 2020; Echeverri et al., 2020). ~~For these data mass scales within a scaling exponent range of $\kappa = 2.2 - 2.6$ (grey area). The chosen mass scaling exponent of $\kappa = 2.4$ is represented by a dashed line and the modeled design~~

4.4 ~~Ground station model~~

~~The ground station is not explicitly modeled in our investigation, but implemented as a set of constraints which play a decisive role in the generated power of ground-generation AWES. Using a simplified model, optimal reel-out speed can be estimated from elevation θ~~ ε ~~and azimuth angle ϕ:~~

$$v_{\text{out}} \approx \frac{1}{3} \cos\theta\varepsilon \cos\phi v_{\text{wind}}. \tag{6}$$

~~(Section 5.5). Therefore, reel-out speed is expected to remain below $10\ \text{ms}^{-1}$ as the wind speed hardly exceeds $20\ \text{ms}^{-1}$. A reel-out speed of $v_{\text{out}} = 15\ \text{ms}^{-1}$ and reel-in speed of $v_{\text{out}} = 10\ \text{ms}^{-1}$ were chosen, resulting in a reel-out to reel-in ratio of $\frac{2}{3}$ which is assumed to be within design limitations. A maximum tether acceleration of $\ddot{l} = 20\ \text{ms}^{-2}$ is imposed to comply with generator torque limits. The tether diameter is chosen such that rated power is achieved at $U_{\text{ref}} = 10\ \text{ms}^{-1}$. Tether force~~

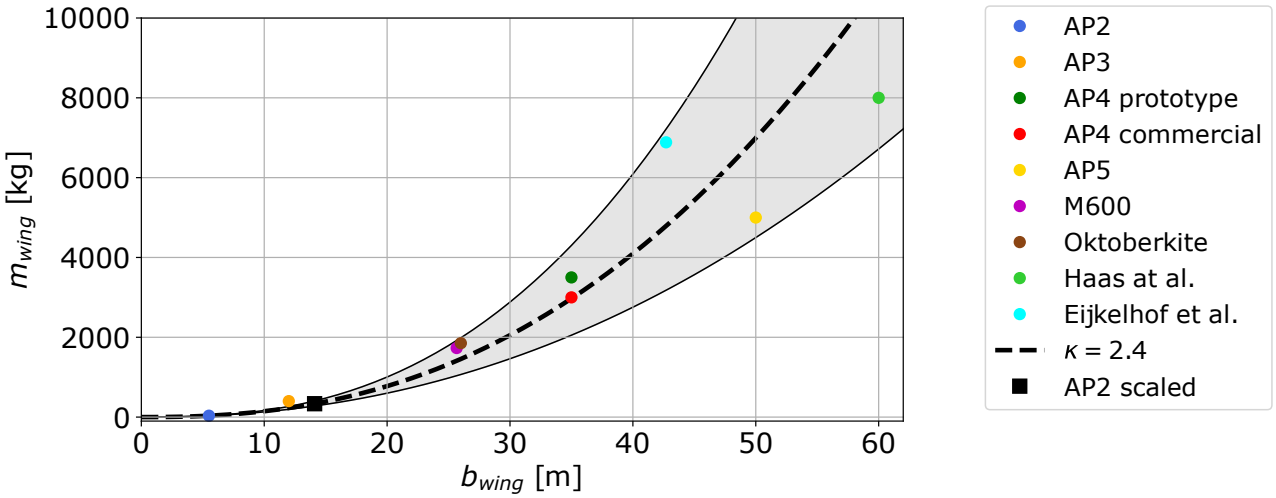

Figure 11. Curve fit of published sizing studies AWES aircraft mass (Haas et al., 2019; Kruijff and Ruiterkamp, 2018; Eijkelhof et al., 2020; Ampyx, 2020; Echeverri et al., 2020). For these data mass scales within a scaling exponent range of $\kappa = 2.2 - 2.6$ (grey area). The chosen mass scaling exponent of $\kappa = 2.4$ is represented by a dashed line and the investigated scaled AP2 design is highlighted by a black square.

~~constraints enforce tension to remain positive whilst not exceeding the maximum tether stress, to which a safety factor of 3 is applied. This results in a tripling of the cross-sectional tether area. These ground station and tether constraints do not represent a fully optimized AWES, but rather a representative system.~~

5 Optimal control problem

Sub-section 5.1 introduces the dynamic trajectory optimization `awebox` model (De Schutter et al., 2020). This is followed by a description of the applied constraints (Sub-section 5.2), the implementation of wind profiles (Sub-section 5.3) and solution method (Sub-section 5.4) of the optimal control problem. A simple quasi steady-state (~~QSS~~ QSM) AWES model (Sub-section 5.5) and a steady-state WT model are also introduced to compare and validate the optimization results and serve to illustrate the limitations of simplified models for performance prediction of AWES.

5.1 AWES model overview

AWES need to dynamically adapt to changing wind conditions to optimize power generation. This can be formulated as a trajectory optimization problem which combines the interaction between tether, flying wing and ground station. For the purposes of this study, we analyze the mechanical power produced by a single tethered aircraft and assume a straight, ~~rigid~~ straight tether. Generating dynamically feasible and power-optimal AWES flight trajectories for given wind profiles is a nontrivial task given the nonlinear and unstable system dynamics and the presence of nonlinear flight envelope constraints. Optimal control

methods are a natural candidate to tackle this problem, given their inherent ability to deal with nonlinear, constrained multiple-input-multiple-output systems. In periodic optimal control, an optimization problem is solved to compute periodic system state and control trajectories that optimize a system performance index (here average AWES power output $\overline{P}$) while satisfying the system dynamic equations. The initial and final state of the trajectory are freely chosen by the optimizer but must be equal to ensure periodic operation. We ~~here~~ apply this methodology here to generate realistic single-wing, ground-generation AWES power curves and AEP estimation based on WRF-simulated wind velocity profiles using the `awebox`. Other wind data sets, such as from a wind atlas, LiDAR campaign or met mast measurements can be implemented as well, depending on the scope and purpose of the investigation. Take-off and landing are not considered. Instead, only the production cycle, including reel-out as well as reel-in period, is optimized.

5.2 Constraints

The tether constraints such as tether length, speed and force are summarized in Table 3. Flight envelope constraints include limitation of aircraft acceleration, roll and pitch angle (to avoid collision with the tether) and angle of attack. The lift coefficient is assumed to be linear within this range. Furthermore, a minimal operating height of $z_{\min} = 50 + \frac{A_{\text{wing}}}{2}$ m is imposed for safety reasons.

Table 3. Aircraft design parameters for AWES $A_{\text{wing}} = 20$ m^2 analyzed in this study and for the original AP2 aircraft. Values in square brackets represent flight envelope bounds, which are implemented as inequality constraints of the optimization.

	Parameter	AP2	design 1
Aircraft	~~wing area~~ A [m^2]	3	20
	~~wing chord~~ c_{wing} [m]	0.55	1.42
	~~wing span~~ b_{wing} [m]	5.5	14.1
	~~wing~~ AR [-]	10	10
	~~kite mass~~ m_{aircraft} [kg]	36.8	355
	α [°]		[-10 : 30]
	β [°]		[-15 : 15]
	~~max. air speed [ms^{-1}]~~		~~75~~
Tether	~~max. length~~ l [m]		2000
	~~speed~~ $\dot{l}$ [ms^{-1}]		[-15 : 10]
	~~max. acceleration~~ $\ddot{l}^{\max}$ [ms^{-2}]		[-10 : 10]
	~~diameter~~ d [mm]		7.8
	~~max. stress [Pa]~~ $\sigma^{\text{tether}}_{\max}$ [Pa]		3.6×10^9
	~~max. force [kN]~~ $F^{\max}_{\text{tether}}$ [kN]		60
	~~min operating altitude [m]~~ $z^{\min}_{\text{operating}}$ [m]		60

5.3 Wind profile implementation

Representative wind velocity profiles derived from WRF, described in Section 2 and clustered in Section 3, are implemented into the trajectory optimization framework (Section 4) to determine optimal trajectories, mechanical AWES power and derive power curves. These results are referencesd against AWES performance subject to a standard logarithmic wind speed profile. The 2D wind components are rotated such that the main wind direction (u_{main} as defined by the average wind direction up to 500 m, compare Section 3) is in positive x-direction and the ~~deviation from it~~ transverse component in y-direction. This is equivalent to assuming omnidirectional AWES operation with the wing still needing to adjust to changing wind conditions with height. Furthermore, we include a simplified atmospheric model based on international standard atmosphere to account for air density variation.

AWES trajectories depend on prevailing wind conditions as they greatly benefit from continuously adapting their operational altitude, tether reeling speed and flight path to maximize power production and minimize losses. Within each cluster, three WRF-calculated wind velocity profiles are chosen and implemented into the trajectory optimization framework. To that end, wind velocity profiles are sorted based on the average wind speed up to 500 m, ~~which is used as an a priori proxy for operating height.~~ From these sorted wind profiles, the 5th, 50th and 95th percentile profile are chosen and assumed to be representative of the spectrum of wind conditions within this cluster. These three wind profiles of every cluster function as boundary conditions in the dynamic optimization model ~~(Section 5~~ and are used in the simplified ~~QSS~~ QSM ~~model (Sub-section 5.5).~~ To implement the wind velocity profile into the optimization framework, the u- and v-components of the wind velocity ~~profile~~ are interpolated individually using Lagrange polynomials. Lagrangian polynomials ~~were~~ are chosen because the function passes through the data points, but any other polynomial could have been chosen as long as the derived function is twice continuously differentiable. This is necessary to implement them into the optimal control problem that can be solved with the gradient-based nonlinear programming (NLP) solver IPOPT (Waechter and Laird, 2016). ~~Therefore, the analyses in Section 6 are based on three wind profiles for each of the k=5, 10, 20, 50 clusters (Section 3)~~ Later analyses are based on three wind profiles for each of the k=5, 10, 20, 50 clusters.

For comparison, logarithmic wind speed profiles ~~(Equation (7))~~, with a roughness length of $z_0^{\text{onshore}} = 0.1$ and $z_0^{\text{offshore}} = 0.001$, are implemented into the trajectory optimization framework

$$U_{\log} = U_{\text{ref}} \left(\frac{\log_{10}(z/z_0)}{\log_{10}(z_{\text{ref}}/z_0)} \right). \tag{7}$$

The reference wind speed U_{ref}, at reference height $z_{\text{ref}} = 10\,\text{m}$, varies from 3 to 19 ms^{-1} with a step size of $\Delta U_{\text{ref}} = 2\,\text{ms}^{-1}$.

5.4 Problem formulation and solution

AWES trajectory optimization is a highly nonlinear and non-convex problem which ~~likely has~~ can have multiple local optima. Therefore, the particular results generated by a numerical optimization solver can only guaranty local ~~optimally~~ optimality,

and usually depend on the chosen initialization. This can result in unwanted or unrealistic AWES trajectories, which implies that the quality of all solutions needs to be evaluated a posteriori.

A periodic optimal control problem is formulated to maximize the average cycle power $\overline{P}$ of a single AWES subject to equality (e.g. tether diameter) and inequality constraints described above (De Schutter et al., 2019; Leuthold et al., 2018). The trajectory optimization problem is discretized into 100 intervals using direct collocation.

An initial guess is generated using a homotopy technique similar to Gros et al. (2013). A circular trajectory is estimated based on a fixed number of loops (here $n_{\text{loop}} = 5$) at a 15° elevation angle and the initial tether length. Initial aircraft speed is based on the estimated duration of a single loop (here 10 sec). Previous analyses showed that the `awebox`-estimated power output is insensitive to the number of loops and therefore ~~flight time~~ cycle duration, at least for less than 10 loops. The homotopy technique initially fully relaxes the dynamic constraints using fictitious forces and moments to reduce model nonlinearity and coupling, improving the convergence of Newton-type optimization techniques. The constraints are then gradually re-introduced until the relaxed problem matches the original problem. The resulting nonlinear program (NLP) is formulated in the symbolic modeling framework CasADi for Python (Andersson et al., 2019) and solved using the linear solver MA57 (HSL, 2020) in IPOPT (Wächter and Biegler, 2006).

5.5 Engineering reference models

AWES power production is intrinsically linked to the aircraft's flight dynamics, as the AWES never reaches a steady state over the course of a power cycle. The ~~employed QSS~~ ground-generation ~~AWES model (Equation (8))~~ QSM is based on Argatov et al. (2009) and has been generalized by Schmehl et al. (2013) to include losses arising from misalignment of the tether and wind velocity vector. The aircraft is represented by a point mass. Its position is described in the spherical coordinates by the distance from the ground station, the elevation angle ε and azimuth angle ϕ relative to the wind velocity vector. The QSM is based on the assumption that the flight of a kite can be approximated by a progression through steady equilibrium (quasi-steady) states. For lightweight kites, this is a reasonably good approximation, because the low mass of the kite leads to very short acceleration times. ~~, adapted from Loyd's crosswind power approximation~~ (Loyd, 1980)~~, simplifies the complex trajectory of a rigid body to a single point mass in a state of equilibrium, pointing directly crosswind.~~

$$P_{\text{optmax}} = \frac{\rho_{\text{air}}(z)}{2} A_{\text{wing}} U^3(z) c_{\text{R}} \left(\frac{c_{\text{R}}}{c_{\text{D,total}}} \right)^2 f_{\text{opt}} \left(\cos\theta\varepsilon \cos\phi - f_{\text{opt}} \right)^2 \tag{8}$$

$$c_{\text{R}} = \sqrt{c_{\text{L}}^2 + c_{\text{D,total}}^2} \tag{9}$$

~~Optimal~~ Power P_{optQSM} described as a function of wind speed U, air density ρ_{air} and the resultant aerodynamic force coefficient c_{R} ~~(Equation (9))~~, which is calculated from the aerodynamic lift c_{L} and total drag coefficient $c_{\text{D,total}}$, including wind~~d~~g and tether drag. Aircraft and tether mass are neglected. The ~~QSS~~ QSM ~~model~~ is subject to the same representative, simulated WRF wind profiles as the dynamic optimization framework.

Under ideal conditions, this model predicts optimal instantaneous power for a given AWES design, kite position (ε, ϕ) and reeling factor f and wind conditions. The QSM predicts power for every operating height and angle of attack. Based on these results, maximum power of every wind speed profile is determined. Reel-in losses are neglected, because we assume tether tension to be negligible during this phase. ~~For every wind speed profile maximum power is determined by varying operating height and angle of attack. We assume the AWES to produce optimal power throughout the entire reel-out phase and neglect reel-in losses, because of negligible tether tension during reel-in. Aircraft and tether mass are neglected.~~ Tether speed $v_t \dot{l}$ is non-dimensionalized in the form of the reeling factor ($f = \frac{v_t}{U}$) and assumed to take the optimal value of ~~$f_{opt} = \frac{1}{3} \cos\theta_\varepsilon \cos\phi$.~~

$$f_{opt} = \frac{1}{3} \cos\theta_\varepsilon \cos\phi \tag{10}$$

, which can be derived from Equation (8) by a simple extreme value analysis The aircraft is assumed to move directly crosswind with a zero azimuth angle $\phi = 0$ relative to the wind direction. All aerodynamic forces and the tether tension act on the single point mass and result in an equilibrium state. The elevation angle $\theta_\varepsilon = \arcsin(\frac{z}{l_{tether}})$ is derived from altitude z and tether length l_{tether} and describes the losses associated with the misalignment between an assumed horizontal wind direction and an inclined tether. The total drag coefficient $c_{D,total}$ determines the aerodynamic drag of the entire AWES, comprising kite and tether, in crosswind motion. It ~~highly~~ strongly depends on the tether diameter d_{tether} and length l_{tether}, as well as the wing area A_{wing} and its aerodynamic drag coefficient $c_{D,wing}$ defined by the ~~wing shape~~ angle of attack and the shape of the wing. A tether diameter $d_{tether} = 7.8$ mm is chosen such that rated wind speed is achieved at $v_{rated} = 10\ ms^{-1}$ (Table 3).

Beyond rated wind speed, tether length, operating height and angle of attack are chosen to stay within the constraints (see Sub-section 5.2) which apply to both the dynamic optimization model and the ~~QSS~~ QSM ~~model~~.

Additionally, optimization results are referenced against a simple steady-state WT model

$$P_{WT} = c_p^{WT} \frac{1}{2} \rho_{air} A_{WT} U^3 (z_{WT} = 100\ m). \tag{11}$$

The hub height z_{WT} is assumed to be 100 m for both onshore and offshore WT. The rotor diameter $D_{WT} \approx 35m$ and swept area of the turbine $A_{WT} \approx 1425m^2$ ~~is~~are chosen such that rated power, at a rated wind speed of $v_{rated} = 10\ ms^{-1}$, is equivalent to AWES rated power $P_{rated} = 260kW$, assuming a constant power coefficient of $c_p^{WT} = 0.45$.

6 Results and discussion

This section describes AWES trajectories and time series (Sub-section 6.1) results generated by the trajectory optimization toolbox ~~(Section 4)~~ and compares them to a quasi-steady reference AWES model ~~(Sub-section 5.5)~~. ~~Wind boundary conditions are based on simulated onshore (Pritzwalk) and offshore (FINO3) wind data (Section 2). Representative wind velocity profiles have been chosen from clustered wind data (Section 3).~~ Sub-section 6.2 examines operating height statistics and tether length trends. ~~Lastly, we~~ Sub-section 6.3 compares AWES performance in terms of power curve ~~(Sub-section 6.3)~~. ~~and annual energy~~

production (AEP) (Sub-section 6.4). These results are analyzed for $k = 20$ clusters, based on the results of the previously described elbow method and silhouette score (Section 3). Lastly, we compare the impact of number of clusters on predicted AEP.

6.1 Flight trajectory and time series results

This sub-section offers insight into typical optimized AWES flight trajectories. Figures 12 and A4 **Roland: Why do you put this into the appendix? The appendix should contain only supplementary material, but I would not have the reader now having to jump back and forth to follow the discussion. Markus: I put the figure in the appendix because I thought that there already are many figures in the paper. We can move it here if you think it is better this way.** compare the trajectories of representative onshore and offshore wind conditions between typical low and high wind speeds for an aircraft with a wing area of $A_{\text{wing}} = 20\ \text{m}^2$. These trajectories and wind velocity profiles have only been chosen to visualize the range of wind conditions and the resulting trajectories. They do not depict special circumstances. They depict common trajectories.

Figure 12 and A4 show the wind speed profiles U over altitude z (a) with the operating height highlighted in color. The colored segments also depict the Lagrange polynomials that interpolate the WRF simulation data for optimization purposes. Sub-figure c Figure 12 (c) shows a top view of the wind velocity profile (rotated horizontal u_{main} and $u_{\text{deviation}}$ wind component) in grey up to 1000 m displayed above as well as the part of the profiles corresponding to the height range swept by the aircraft in color. The two center plots in the middle column show the optimized trajectory in side view (b, $x - z$ plane) and top view (d, $x - y$ plane).

When maximum tether force is reached the system starts to de-power while maintaining the same high tension (Sub-figure e in Figures Figure 12 (e) and Figure A4 (e)). Such trajectories often extend perpendicular to the main wind direction or increase the elevation angle, while maintaining a constant, maximum tether tension This often results in odd or unexpected trajectories, even though these local minima are within the system constraints (roll rate etc.). De-powering by increasing the elevation angle is also possible and likely to happen, but harder to determine as it is not easily identifiable whether the elevation angle increased due to better wind conditions or to de-power the wing. Reducing the angle of attack Figure 12(g) while maintaining constant maximum tether force Figure 12(e) can be observed in the highest onshore wind speed trajectory (green). During the production loops, the angle of attack constraint of the red and orange trajectories are active. The AWES angle of attack at the onshore location is generally higher than offshore (Sub-figureSub-figure c Figure 12 (c) shows a top view of the wind velocity profile (rotated horizontal u_{main} and $u_{\text{deviation}}$ wind component) in grey up to 1000 m displayed above as well as the part of the profiles corresponding to the height range swept by the aircraft in color. Sub-figure c Figure 12 (c) shows a top view of the wind velocity profile (rotated horizontal u_{main} and $u_{\text{deviation}}$ wind component) in grey up to 1000 m displayed above as well as the part of the profiles corresponding to the height range swept by the aircraft in color. g in Figure 12(g) and Figure A4 (g)). This can likely be attributed to the fact that onshore tether lengths are generally longer than offshore, where beneficial wind conditions allow the AWES to operate at lower altitudes Section 6.2. As a result, the optimal $c_{\text{L}}^3/c_{\text{D}}^2$ shifts towards higher angle of attack.

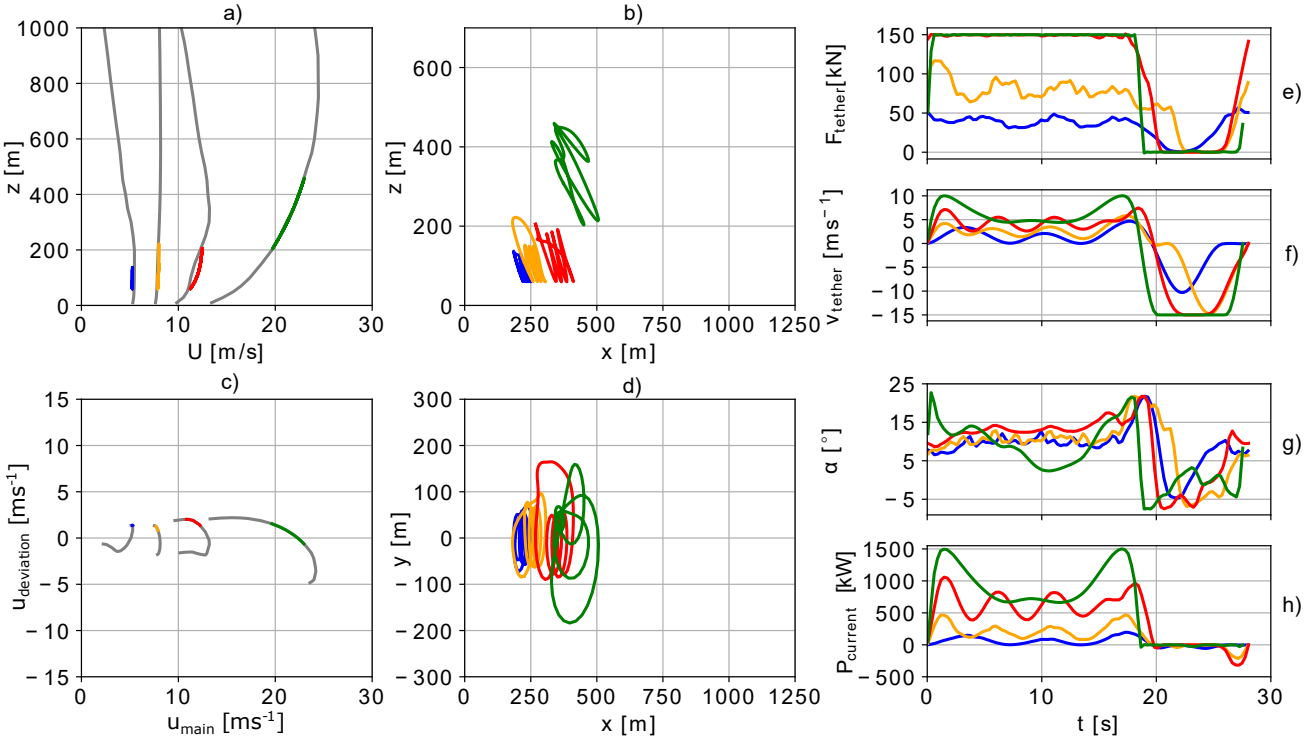

Figure 12. Representative wind speed profiles (a), and hodograph (top view) of wind velocity up to 1000 m (c). Wind profiles chosen to represent typical low (blue, orange), medium (red) and high wind speeds (green). Trajectories (b,d) in side and top view. Temporal variations of tether force F_{tether} (e), tether reeling speed $v_{\text{tether}}\dot{l}$ (f), angle of attack α (g) and instantaneous power P_{current} (h) optimized based on clustered onshore wind speed profiles for a ground-generation AWES with a wing area of $A_{\text{wing}} = 20\ \text{m}^2$.

The optimal control algorithm seems to always maximize tether force and vary tether reeling speed Figure 12(f) close to optimal reel-out speed ($v_{\text{out}} \approx \frac{1}{3} v_{\text{wind}} \dot{l}_{\text{out}} \approx \frac{1}{3} \cos\varepsilon \cos\phi$ (Loyd, 1980)) to maximize average cycle power. At high wind speeds, the trajectory starts to differ from its predefined shape with distinct loops and the system de-powers, which can be seen in the power development during the production phase (green). Trajectories for such high speed wind conditions without a tether force constraint, where the tether diameter is adjusted to the wind conditions, would be closer to the looping paths seen for lower wind speeds (blue, orange, red). The optimizer tries to keep the reel-in phase as short as possible, given tether speed and acceleration constraints. As a result, the reel-in tether speed reaches its limit for high wind speeds. The time history of instantaneous power P_{current} Figure 12(h) clearly distinguishes the production and consumption phases of pumping-mode (ground-generation) AWES.

All optimized trajectories have a close to zero power usage during reel-in as they reduce the angle of attack to near zero lift conditions. One commonality between all time series is that they almost all have the same ~~flight time~~ cycle duration independent

of location, wind speed or aircraft size. The ~~flight time~~ cycle duration is almost solely determined by the initial number of loops, here five, used in the initialization procedure. This is likely a result of the optimization algorithm. ~~The optimized trajectories result in almost zero tether force, and therefore energy consumption, during the reel-in phase.~~ Based on previous analyses, net mechanical AWES power output seems to be insensitive to the number of loops and ~~flight time~~ cycle duration. This might be different for real deployment, where a higher number of loops could be beneficial, because the reel-in time relative to reel-out time could be shorter.

6.2 Tether length, elevation angle and operating altitude

This sub-section compares tether lengths and operating altitudes for a wing size of $A_{\text{wing}} = 20\ \text{m}^2$. Data are based on 60 wind velocity profiles from $k = 20$ clusters, a reasonable choice based on previous analyses (Section 3), both onshore (Pritzwalk) and offshore (FINO3) ~~(Sub-section 5.3)~~. Within every cluster the p5, p50, p95-th wind profiles ~~is~~are chosen to represent the range of wind conditions aggregated in this cluster.

Figure 13 (a) illustrates the range of onshore (blue) and offshore (orange) ~~AWES~~ tether lengths l_{tether} of each wind velocity profile. The ~~maximum is and minimum~~ maxima and minima are, highlighted by ~~a square,~~ squares and are plotted over reference wind speed $U(z_{\text{ref}} = 100 - 400m\ \text{m})$ Neither of the optimizations reaches the maximum tether length of $l_{\text{tether}}{}^{\text{max}} = 2000\ \text{m}$. Both locations show a trend towards longer tether lengths until rated wind speed. Beyond rated wind speed, tether lengths stay constant or even decrease as the system de-powers and tries to stay within constraints. The slightly lower tether length offshore is probably due to lower wind shear and more homogeneous wind regime (Sub-section 2.2). The onshore data set displays multiple outliers, probably due to wind velocity profile variation, further supporting the need to dynamically adapt AWES operating conditions.

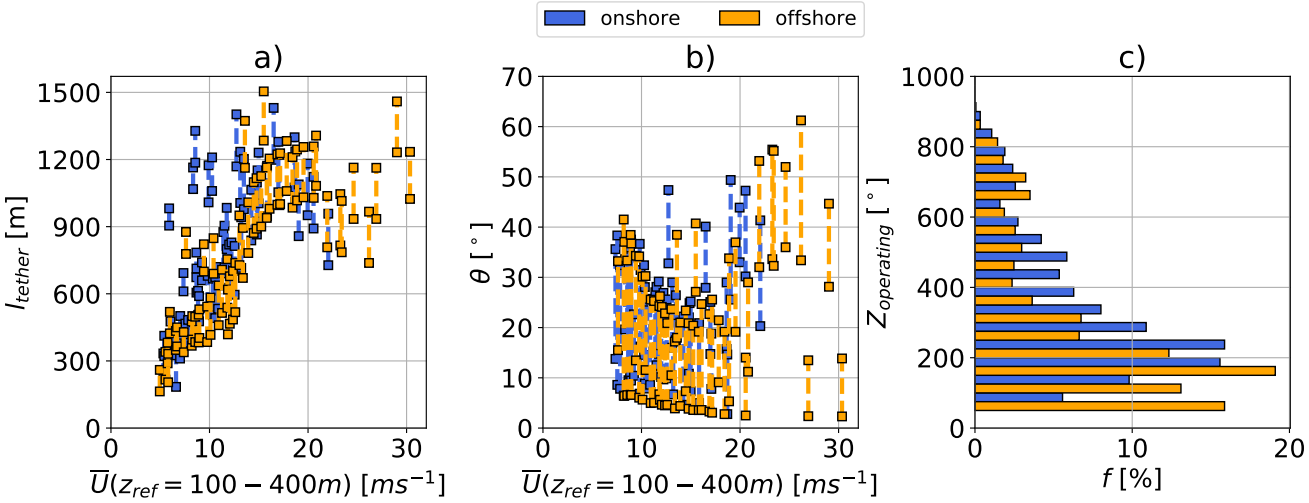

Figure 13. Tether length range (a) over reference wind speed $U(z_{\text{ref}} = 100 - 400\ \text{m})$ and frequency distribution of operating altitude (b) based on `awebox` trajectory optimization of k=20 onshore (blue) and offshore (orange) clusters.

~~Sub-figure~~ Figure 13 (c) shows the elevation angle $\theta\varepsilon$ as a function of reference wind speed $U(z_{\text{ref}} = 100 - 400m\ \text{m})$. As expected, the optimizer tries to keep elevation angle low to reduce misalignment (cosine) losses between the tether and the horizontal wind velocity vector. However, the tether length increase with wind speed leads to an overall increase in operating heights. Both onshore and offshore follow a similar trend.

~~The right side of the~~Figure 13 (c) shows the frequency distribution of operating altitude $z_{\text{operating}}$, calculated from the trajectory, as described in Sub-section 6.1. Operating altitudes over the entire wind regime, both off- and onshore, are almost never higher than 500 m above ground, confirming findings in Sommerfeld et al. (2019a, b). Optimal operating heights at both locations ~~is~~ are below 400 m for almost 78 % of the year. Larger or multi-~~wing~~kite AWES could benefit from higher operating altitudes due to their higher lift to tether drag ratio and weight ratio, but more detailed analyses are required.

6.3 Power curve

This subsection compares power curves derived from power-optimal trajectories, subject to clustered WRF profiles or logarithmic profiles (Sub-section 5.3), to ~~QSS~~ QSM modeled power as well as a WT reference. Furthermore, the impact of different reference heights on AWES power curves, wind speed probability and annual energy distribution is illustrated.

Figure 14 (a, b) shows optimized AWES power based on onshore (blue) and offshore (orange) k=20 clustered WRF profiles (data points), with a least square fit (dashed line). Optimized AWES power based on logarithmic wind speeds (Equation (7)) with a roughness lengths of $z_0^{\text{onshore}} = 0.1$ and $z_0^{\text{offshore}} = 0.001$ (Sub-section 5.3) are depicted as dotted lines. These data are compared to AWES ~~QSS~~ QSM ~~model~~ (solid line) as well as a simplified WT model (red line) described in Sub-section 5.5, both of which use the same clustered WRF wind velocity profiles as the dynamic optimization model. The cut-in wind speed of 5 ms^{-1} is the result of unconverged optimizations below this threshold. No cut-out wind speed was defined. Therefore, energy conversion is only limited by the wind resource. The presented AWES and WT reach rated power around $U_{\text{rated}} \approx 12\text{ms}^{-1}$. To simplify the readability and applicability of the methodology, as well as to be consistent with the power curve definition of conventional wind turbine, a single reference wind speed is chosen to represent the complex wind conditions. We chose average wind speed between 100 and 400 m as reference wind speed (abscissa) because the optimized AWES trajectories mostly operate in this height range (Sub-section 6.2). The shape of the power curve changes depending on reference height which further illustrates the importance of standard AWES reference wind conditions. For the calculation of WT wind speed and energy distribution a reference height of 100 m is used. The clustered power curve fit aligns well with optimization results for logarithmic wind speed profiles at this reference height.

The power harvesting factor ~~(Equation (12))~~ (Diehl, 2013), shown in ~~sub-figures~~ Figures 14 (c) and (d), expresses the estimated AWES power P relative to the total wind power through an area the same size as the wing P_{area}. It can be derived from (8) by setting the elevation angle ε and the azimuth angle ϕ to zero. An extreme value analysis results in an optimal

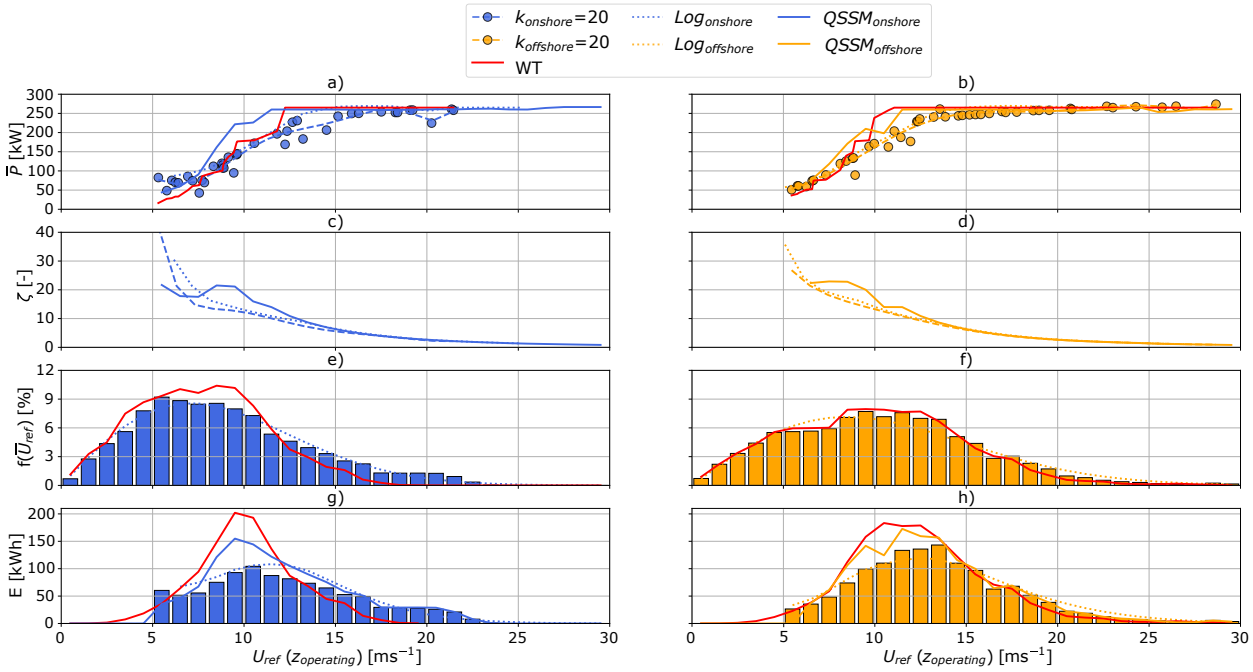

Figure 14. Onshore (blue) and offshore (orange) AWES power curves (a,b) over average wind speed at operating height based on 3 wind profiles for each of the k=20 clusters. Simplified WT model (red lines), ~~QSS~~ QSM AWES model (solid lines) and AWES subject to logarithmic wind boundary conditions (dotted lines) with rated wind speed of $v_{\mathrm{rated}} = 10\ \mathrm{ms}^{-1}$ and the same rated power for reference. Power harvesting factor ζ ~~(Equation (12))~~ shown in c, d. Annual energy distribution (e,f) based on power curves and WRF-simulated annual wind speed probability distributions (c,d) and standard Rayleigh distributions. (IEC, 2010).

reel out speed $\dot{l}$ of 1/3 of the wind speed U (Equation (10)) and $\zeta_{max} = \frac{4}{27} c_{\mathrm{R}} \left(\frac{c_{\mathrm{R}}}{c_{\mathrm{D}}}\right)^2$. P_{area} is not a physical power, but a mathematical concept to non-dimensionalize power.

$$\zeta = \frac{P}{P_{\mathrm{area}}} = \frac{P}{\frac{1}{2}\rho_{\mathrm{air}} A_{\mathrm{wing}} U(z) U_{\mathrm{ref}}{}^3} \leq \frac{4}{27} c_{\mathrm{R}} \left(\frac{c_{\mathrm{R}}}{c_{\mathrm{D}}}\right)^2 \tag{12}$$

ζ is calculated with the average wind speed between $U_{\mathrm{ref}}(z = 100m - 400\ \mathrm{m})$ as a proxy for operating heights. At low wind speeds the optimization model finds higher power output than the ~~QSS~~ QSM ~~model~~. This is likely caused by the choice of reference wind speed which leads to a shift in these data points towards lower wind speeds.

~~Sub-figures e and f~~ Figures 14 (e) and (f) show the wind speed probability distribution for the chosen average reference wind speeds between 100 and 400 m (bars), at 100 m WT hub-height (red line) and the standard Rayleigh distribution (dotted lines) with $U^{\mathrm{ave}}_{\mathrm{onshore}} = 10\ \mathrm{ms}^{-1}$ and $U^{\mathrm{ave}}_{\mathrm{offshore}} = 12\ \mathrm{ms}^{-1}$ ~~(Equation (15))~~. As expected, higher operating altitudes ~~reach~~ are

associated with higher wind speeds. However, ~~low~~ wind speeds ~~of less than~~ below $5\ \mathrm{ms}^{-1}$ still occur almost at the same frequency ~~as at lower altitude~~ at every height, both onshore and offshore.

These distributions, together with the power curves, are used to generate the annual energy distribution in ~~sub-figures g and h~~ Figures 14 (g) and (h). In comparison to conventional WT, the AWES energy distribution is shifted towards higher wind speeds. For AWES to convert power during these conditions, the flight path needs to be adjusted to de-power so that the AWES stays within material strength limitations.

In contrast to conventional WT with ~~their~~ fixed hub-height, AWES adapt their operating heights dynamically, which makes the choice of reference a wind speed non-trivial. Due to many conceptually different AWES designs and the novelty of the technology, ~~no generally accepted~~ various AWES power curve definition exists. Similarly, no standard wind resource model such as the Rayleigh or Weibull distribution for conventional wind has been defined. The AWE glossary (Airborne Wind Europe, 2021) describes the power curve using the average cycle power and pattern trajectory height, which are also used in this research. Figure 15 investigates the impact of different reference heights on AWES ~~power curve representations (a,b)~~ performance characterization.

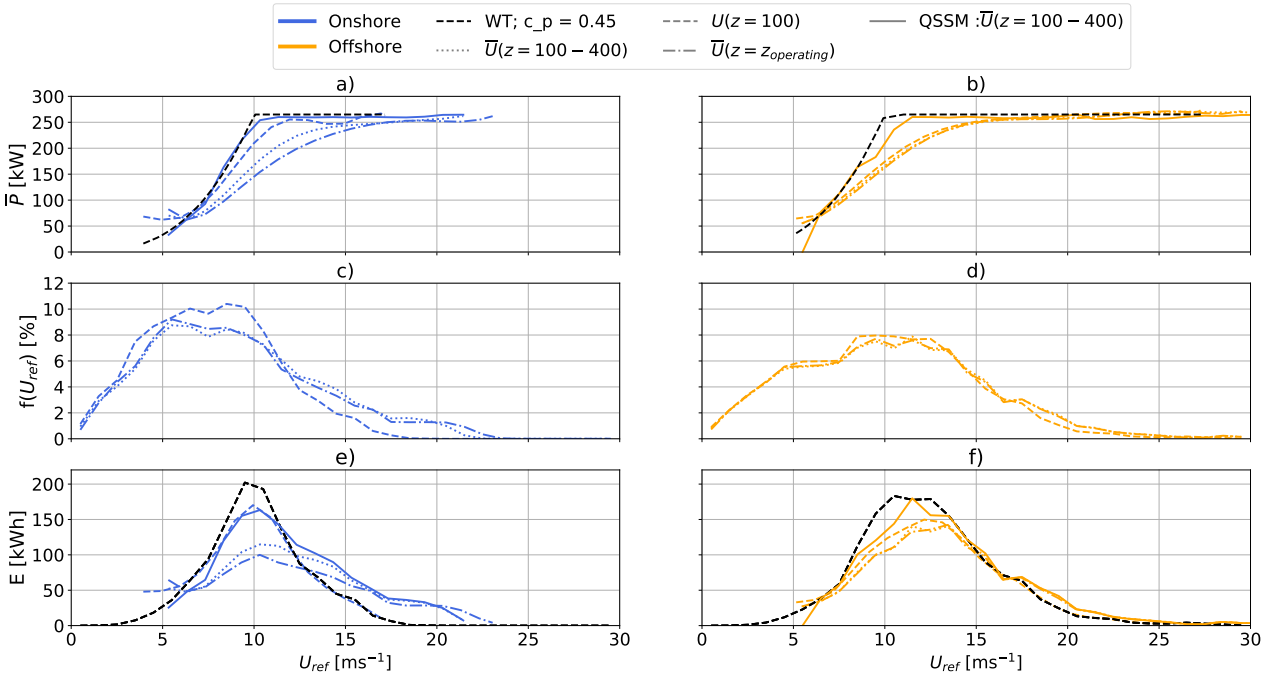

Figure 15. Onshore (blue) and offshore (orange) AWES power curves (a,b) over various reference wind speeds (dashed lines: fixed height $z = 100$ m; dotted lines: $z = 100 - 400$ m; dash-dotted lines: average wind speed along operating trajectory) based on 3 wind profiles for each of the k=20 clusters. A simplified WT (dashed black lines) and ~~QSS~~ QSM AWES model (solid line) with same rated power are depicted as reference. Power curves and WRF-simulated annual wind speed probability distribution (c,d) for various reference heights result in annual energy production distribution (e,f) and AEP estimates.

These power curves in Figures 15 (a) and 15 (b) are derived from curve fits of 3 three wind velocity profiles within each of the k=20 onshore (blue) and offshore (orange) wind speed profile clusters. Together with differing the wind speed probability distributions in Figures 15 (c) and 15 (d)(c,d) this leads to varying annual energy distribution (e,f) in Figures 15 (e) and 15 (f) and therefore AEP (Sub-section 6.4). The area underneath integral of the distribution accumulates to yields the annual energy production (AEP) further analyzed in Sub-section 6.4. WT data with a reference wind speed at $z = 100\text{m}$ (black dashed lines) and QSS QSM data with an average reference wind speed between $100 \leq z \leq 400\text{m}$ (solid lines) are included for comparison.

The presented AWES and WT start producing significant power at around $U \approx 5\ \text{ms}^{-1}$ and reach rated power between 12 and 15 ms^{-1} at their respective reference heights. Whereas the onshore AWES power curve with a fixed reference height of 100 m almost aligns with the power curve of a conventional wind turbine, other power curves are seemingly below that. This is likely caused by higher wind shear and non-monotonic wind speed profiles which lead to faster winds aloft and higher operating altitudes with lower wind speeds at 100 m. For monotonically increasing wind speeds this leads to data points moving to the right when plotted against $u_{100-400\text{m}}$ in comparison to when they are plotted against $u_{100\text{m}}$. Offshore winds however experience less shear (see Sub-section 2.2), which is why offshore AWES power curves for any reference height almost overlap with each other practically coincide. AWES energy production distribution is shifted towards higher wind speeds, particularly onshore, due to higher average wind speeds at operating height. Furthermore, the distribution of AWES energy production shows a wider spread as the system operates within a wider range of wind speeds.

6.4 Annual Energy Production

Long-term wind statistics are necessary to accurately determine reliable Aannual Eenergy Pproduction. Wind resource assessment guidelines typically recommend multi-year wind measurements and long-term wind data corrections via simulations. We only consider wind data for thea simulated one-year time span (Section 2) to simplify the analyses in this research. AEP (Equation 13) is approximated by the sum of the annual energy distribution shown in Figures 14 and 15, which is the multiplication of cycle-average power $\overline{P}$ and wind speed probability $f(\overline{U}_{\text{ref}})$, binned into n_{bin} bins intervals with $\Delta U_{bin} = 1\text{ms}^{-1}$

$$\text{AEP} = \sum_{\text{i}=1}^{n_{\text{bin}}} \left(\overline{P}_i \cdot f_i(\overline{U}_{\text{ref}})\right). \tag{13}$$

Figure 16 compares several AEP estimations of optimized AWES trajectories based on WRF data as well as logarithmic wind speed profiles (AWES_{log}). These results are referenced compared against AEP predictions using the QSS AWES model ($\text{QSS}(100m \leq z \leq 400\ \text{m})$) and steady-state WT model ($\text{WT}(z = 100\ \text{m})$). We compare the impact of reference height on AEP, since no standard reference height is defined for AWES wind statistics. WRF-based AEP estimates use the wind statistics derived from the one-year WRF simulation at z=100 m, average wind statistics between $100\ \text{m} \leq z \leq 400\ \text{m}$ or average wind statistics along the flight path $z_{\text{operating}}$. These are compared to AEP assessed from the summation of power (Equation (14))

$$\text{AEP} = \sum_{\text{j}=1}^{\text{k}} \sum_{\text{i}=1}^{\text{n}} \left(P_{\text{i,j}}^{\text{interp}}\right) \tag{14}$$

over every n 10-min wind speed profile during the one year simulation ($\mathrm{AWES_{cluster}}$). For this approach, power $P_{i,j}^{\mathrm{interp}}$ is interpolated between p5, p50 and p95 within each cluster k and then added up to an annual total energy. The profiles within each cluster are sorted by wind speed up to 500 m, which is used as an a priori proxy for operating height (Sub-section 5.3). We assume that the cycle-average power represents the average power for this time period. In the case of the previously described logarithmic wind speed profiles, a standard Rayleigh distribution ~~(Equation (15))~~ (IEC, 2010)

$$f_{\mathrm{Rayleigh}} = \frac{2U}{U^{\mathrm{avg}}} \exp - \left(\frac{U}{U^{\mathrm{avg}}} \right)^2 \tag{15}$$

with $U_{\mathrm{onshore}}^{\mathrm{avg}} = 10\ \mathrm{ms}^{-1}$ and $U_{\mathrm{offshore}}^{\mathrm{avg}} = 12\ \mathrm{ms}^{-1}$ at $z = 100$ m is used to estimate AEP ($\mathrm{AWES_{log}}$).

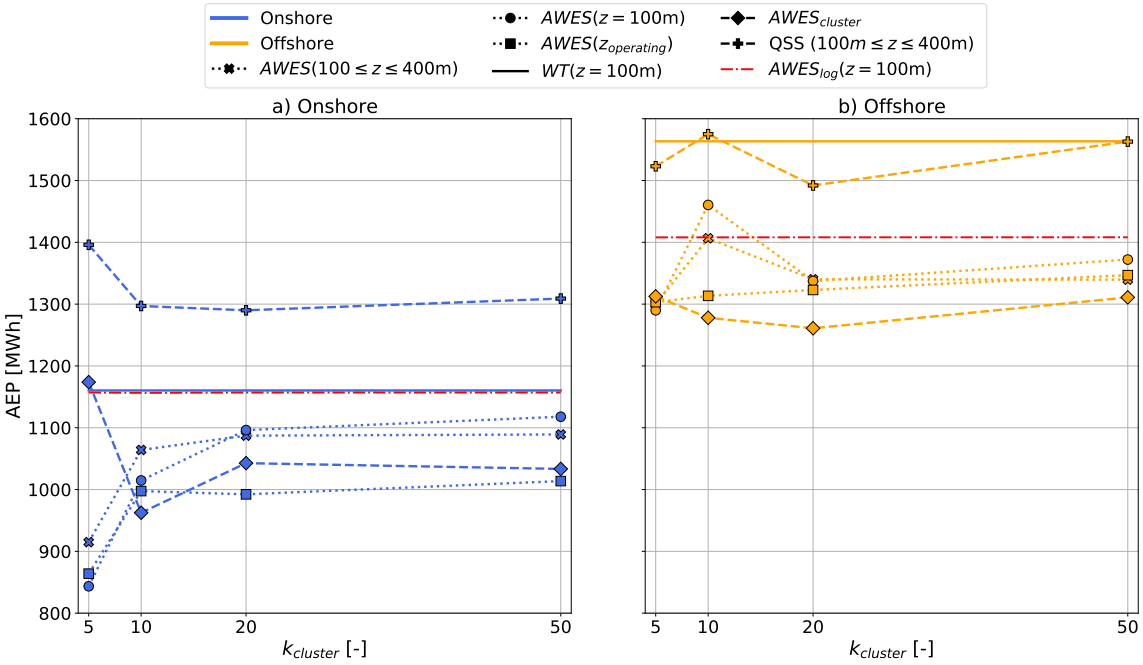

Figure 16. Onshore (a) and offshore (b) AEP over number of clusters k based on power curve and wind speed distribution in Sub-section 6.3 over various reference heights. ~~QSS~~ QSM (+) and WT (solid lines) reference models as well as optimized AWES performance estimated based on logarithmic wind speed profiles (red dash dotted lines) and a Rayleigh distribution at 100 m. $\mathrm{AWES_{cluster}}$ estimates AWES AEP based on the summation of interpolated power within each cluster.

Both onshore (blue) and offshore (orange) AEP vary with number of clusters. However, AEP variation is negligible for more than k=20 and the possible improvement in energy prediction does not justify the increased computational cost. Less wind shear offshore results in decreased spread between reference heights. AEP predictions of $\mathrm{AWES_{cluster}}$ are generally lower than other estimates and closest to $\mathrm{AWES(z_{operating}}$. At both locations, the ~~QSS~~ QSM ~~model~~ overpredicts AEP, due to ~~simplified~~ simplifying assumptions. Onshore, ~~QSS~~ QSM AEP is particularly high, because tether drag might not be accurately

represented, favoring higher operating altitudes. The simplified WT model predicts higher ~~powers~~ AEP than the dynamic optimization AWES model, particularly offshore where lower wind shear only slightly increases energy yield at higher altitudes. Logarithmic wind speed profiles (see Sub-section 5.3) and Rayleigh wind speed probability distributions ($U^{\text{ave}}_{\text{onshore}} = 10\ \text{ms}^{-1}$ and $U^{\text{ave}}_{\text{offshore}} = 12\ \text{ms}^{-1}$) also predict higher AEP than WRF-simulated wind conditions. Offshore AEP estimates based on logarithmic wind profiles are closer to power curve estimates based on WRF data than similar onshore results. This implies that offshore wind conditions (wind profile shape and probability) are better represented by logarithmic wind speed profiles than onshore conditions.

7 Conclusions and outlook

This study derives power-optimal, single-aircraft, ground-generation AWES trajectories and evaluates instantaneous and cycle-average power, annual energy production, operating heights and tether lengths based on representative, mesoscale simulation data. These analyses use both onshore ~~wind~~ simulation data at Pritzwalk in northern Germany and offshore ~~wind~~ simulation data at the FINO3 research platform in the North Sea to drive the AWES optimization framework ~~(~~`awebox`. The~~se~~ mesoscale wind simulations span an entire year with an horizontal grid spacing of 3 km and a temporal resolution of 10 minutes, thereby including seasonal, synoptic and diurnal variations. ~~at a higher resolution than re-analysis data sets.~~ These models are driven by re-analysis data which have a horizontal resolution of approximately 31 km and a temporal resolution of 1-3 hours. The annual wind roses for heights of 100 ~~m~~ and 500 m confirm the expected wind speed increase and clockwise rotation at both locations, with generally lower offshore wind shear and veer than onshore. Annual wind speed statistics reveal that while average wind speeds increase with height, low wind speeds still occur at a fairly high probability up to 1000 m.

To further dissect wind conditions that are essential to the design and operation of AWES and to reduce computational cost, a representative wind resource model is deduced using k-means clustered wind data. This algorithm groups similar profiles together into a fixed, predetermined number of k clusters represented by the mean of each cluster. For a representative k= 10 ~~of 10~~ (chosen for visualization purposes) a more ~~extensive~~ accurate analysis with k=20 and comparison between onshore and offshore wind conditions revealed that average wind speed, rather than profile shape, plays a decisive role in assigning profiles to a certain cluster. The algorithm was able to identify a cluster for onshore LLJs as well as various non-logarithmic wind profiles at both locations. Individual clusters produce coherent groups of similar wind velocity profiles whose probability correlates with seasonal, diurnal and atmospheric stability variation. k-means clustering provides good insight into the wind regime, especially for higher altitudes where classification by Obukhov length is inadequate. Furthermore, the ~~so~~ derived clusters represent annual variation better than conventional logarithmic or exponential wind speed profiles.

Trajectories for three representative wind velocity profiles, selected based on the 5th, 50th and 95th percentile wind speed from each k=5, 10, 20, 50 cluster, as well as logarithmic reference wind speed profiles, are optimized. A scaled Ampyx AP2 aircraft ($A_{\text{wing}} = 20\ \text{m}^2$) is analyzed in terms of trajectory, operating altitude, instantaneous tether force and length as well as power and AEP. The results show that AWESs at both locations rarely operate above 400 m, with offshore systems mostly flying below 200 m, due to higher wind speeds at lower altitude and low wind shear. ~~These results weaken~~ This

weakens the claim in some early airborne wind energy literature of increased power harvest above 500 m for AWES~~, but also obviate airspace restriction challenges for AWES.~~ Our findings inform airspace regulators and companies to address airspace restriction challenge. A simplified quasi-steady state (~~QSS~~ QSM) AWES as well as WT models ~~are~~ were used ~~to contextualize~~ for comparison with the optimization results and functioned as reference for power curve descriptions over various reference heights. The WT model reaches rated power at lower wind speeds, because tether losses decrease AWES power, which the ~~QSS~~ QSM AWES model can not fully capture. Deriving AWES power curves from logarithmic wind speed profiles seems like a valid approach especially offshore. Logarithmic wind speed profiles onshore can not account for the high amount of non-monotonic profiles. ~~Onshore, the choice of reference height can seemingly result in delayed important for the design as it defines rated power as the power curve shifts.~~ The choice of reference height is very important as it defines the power curve and moves cut-in, cut-out and rated wind speed. This is particularly true onshore. ~~This choice is~~ Offshore on the other hand the choice is less significant ~~offshore~~ due to reduced wind shear and more monotonic wind velocity profiles. This choice highly affects AEP predictions and requires further investigation.

Beneficial offshore wind conditions lead to higher ~~AWES~~ AEP than onshore. The WT model generally predicts higher AEP than the investigated AWES models. Onshore the AWES performs better relative to the WT reference, due to higher wind shear. ~~However, onshore AWES predict a higher improvement relative to the WT reference model, which generally predicts higher AEP, due to higher wind shear and higher wind speeds aloft.~~ ~~QSS~~ QSM AWES model AEP estimates are higher than dynamic optimization results, because they do not capture power variation along the flight path and under-predict tether losses. Probably the most realistic, but also lowest energy yield predictions are derived from wind speed distributions at operating height $AWES_{operating}$ and the summation of annual, interpolated power $AWES_{cluster}$. AWES AEP based on logarithmic wind profiles and Rayleigh wind speed distributions predict higher yield than AEP based on clustered WRF-simulated wind resource, indicating that the conventional approach can not reproduce the impact of realistic wind conditions on AWES performance. This is due to the fact that the Rayleigh distribution over-predicts high wind speeds. Comparing WRF-clustered AEP for different power and wind resource descriptions shows that the benefits of using more than k=20 clusters are marginal while computational expense increases. ~~Using~~ The wind speed distribution at a fixed reference height of 100 m leads to an over prediction of ~~annual energy~~ AEP, particularly onshore. Instead, we propose to use the average wind speed between 100 - 400 m to estimate AEP and an apriori guess for pattern height, because AWES mostly operate within this height range. ~~and AEP estimates are closer to AEP of $AWES_{\text{operating}}$ and $AWES_{\text{cluster}}$.~~ The choice of reference height for the derivation of the wind speed probability distribution is more important onshore, due to higher wind shear and more non-monotonic wind speed profiles.

In summary, k-means clustering provides adequate categorization and realistic, representative wind velocity profiles for AWES trajectory optimization. This approach increases the accuracy of AWES power prediction in comparison to logarithmic wind speed profiles. Furthermore, clustering reduces the computational cost of power curve and AEP estimates as a low number of clusters suffices. The choice of reference height impacts the power curve and AEP estimates, further demonstrating the importance of defining adequate AWES standards. Offshore AWES power curves generated based on WRF wind data are similar to power curves based on logarithmic reference model, because non-monotonic wind profile shapes are less common

offshore. Estimating AEP based on wind statistics from a posteriori operating heights or from the summation of interpolated power within each cluster produces similar results. These AEP approximations need to be validated against real AWES AEP data.

Based on these results, we will describe the design space and weight budget of ground-generation AWES in a ~~future~~ parallel sizing study (Sommerfeld et al., 2020) using the clustered wind data. To that end, we will compare the performance of a high-lift airfoil to the baseline AP2 aerodynamic reference model and determine the maximum permissible mass for different wing sizes. In the end, an investigation of measured power curves and real AEP from field trials is necessary to confirm or highlight deficiencies in the models used in this paper. Until then, long-term AWES performance analysis based on mesoscale and reanalysis data are an alternative to estimate AWES AEP. The simple power curve and AEP estimates presented in this research, can be compared to results derived from methods using more detailed numerical integration that take clustering and power optimization into account. The description of the AWES wind resource, particularly onshore, needs further analysis as it highly impacts AWES energy yield predictions. An interesting open research question is the seasonality of AWES performance in comparison to WT.

7.1 Acknowledgments and funding sources

The authors thank the BMWi for funding of the "OnKites I" and "OnKites II" projects [grant numbers 0325394 and 0325394A] on the basis of a decision by the German Bundestag and project management Projektträger Jülich. We thank the PICS, NSERC and the DAAD for their funding.

`awebox` has been developed in collaboration with the company Kiteswarms Ltd. The company has also supported the `awebox` project through research funding. The `awebox` project has received funding from the European Union's Horizon 2020 research and innovation program under the Marie Sklodowska-Curie grant agreement No 642682 (AWESCO).

We thank the Carl von Ossietzky University of Oldenburg and the Energy Meteorology research group for providing access to their high performance computing cluster *EDDY* and ongoing support.

We further acknowledge Rachel Leuthold (University of Freiburg, SYSCOP) and Thilo Bronnenmeyer (Kiteswarms Ltd.) for their help~~ed~~ in writing this article, great, technical support and continued work on the `awebox`.

7.2 Author contribution

Markus Sommerfeld evaluated the data and wrote the manuscript in consultation and under the supervision of Curran Crawford. Martin Dörenkämper set up the numerical offshore simulation, contributed to the meteorological evaluation of the data and reviewed the manuscript. Jochem De Schutter co-developed the optimization model and helped writing and reviewed this manuscript.

References

Airborne Wind Europe: Airborne Wind Energy Glossary, https://airbornewindeurope.org/resources/glossary-2/, last accessed: 2022-03-29, 2021.

Ampyx: Ampyx Power BV, https://www.ampyxpower.com/, 2020.

Andersson, J. A. E., Gillis, J., Horn, G., Rawlings, J. B., and Diehl, M.: CasADi – A software framework for nonlinear optimization and optimal control, Mathematical Programming Computation, 11, 1–36, https://doi.org/10.1007/s12532-018-0139-4, 2019.

Archer, C. L., Colle, B. A., Veron, D. L., Veron, F., and Sienkiewicz, M. J.: On the predominance of unstable atmospheric conditions in the marine boundary layer offshore of the U.S. northeastern coast, Journal of Geophysical Research: Atmospheres, 121, 8869–8885, https://doi.org/10.1002/2016JD024896, 2016.

Argatov, I. and Silvennoinen, R.: Efficiency of Traction Power Conversion Based on Crosswind Motion, in: Airborne Wind Energy, edited by Ahrens, U., Diehl, M., and Schmehl, R., pp. 65–79, Springer, Berlin, Heidelberg, https://doi.org/10.1007/978-3-642-39965-7_4, 2013.

Argatov, I., Rautakorpi, P., and Silvennoinen, R.: Estimation of the mechanical energy output of the kite wind generator, Renewable Energy, 34, 1525–1532, https://doi.org/10.1016/j.renene.2008.11.001, 2009.

Arya, P. and Holton, J.: Introduction to Micrometeorology, International Geophysics, Elsevier Science, 2001.

Aull, M., Stough, A., and Cohen, K.: Design Optimization and Sizing for Fly-Gen Airborne Wind Energy Systems, Automation, 1, 1–16, https://doi.org/10.3390/automation1010001, 2020.

Banta, R. M.: Stable-boundary-layer regimes from the perspective of the low-level jet, Acta Geophysica, 56, 58–87, https://doi.org/10.2478/s11600-007-0049-8, 2008.

Bronnenmeyer, T.: Optimal Control for Multi-Kite Emergency Trajectories, Master's thesis, University of Stuttgart, https://cdn.syscop.de/publications/Bronnenmeyer2018.pdf, 2018.

Carl von Ossietzky Universität Oldenburg: EDDY @ONLINE, https://www.uni-oldenburg.de/fk5/wr/hochleistungsrechnen/hpc-facilities/eddy/, 2018.

Cherubini, A., Papini, A., Vertechy, R., and Fontana, M.: Airborne Wind Energy Systems: A review of the technologies, Renewable and Sustainable Energy Reviews, 51, 1461–1476, https://doi.org/10.1016/j.rser.2015.07.053, 2015.

De Schutter, J., Leuthold, R., Bronnenmeyer, T., Paelinck, R., and Diehl, M.: Optimal control of stacked multi-kite systems for utility-scale airborne wind energy, in: 2019 IEEE 58th Conference on Decision and Control (CDC), pp. 4865–4870, https://doi.org/10.1109/CDC40024.2019.9030026, 2019.

De Schutter, J., Malz, E., Leuthold, R., Bronnenmeyer, T., Paelinck, R., and Diehl, M.: `awebox`: Modelling and optimal control of single- and multiple-kite systems for airborne wind energy, https://github.com/awebox, last accessed: 2021-10-11, 2020.

Dee, D. P., Uppala, S. M., Simmons, A. J., Berrisford, P., Poli, P., Kobayashi, S., Andrae, U., Balmaseda, M. A., Balsamo, G., Bauer, P., Bechtold, P., Beljaars, A. C. M., van de Berg, L., Bidlot, J., Bormann, N., Delsol, C., Dragani, R., Fuentes, M., Geer, A. J., Haimberger, L., Healy, S. B., Hersbach, H., Hólm, E. V., Isaksen, L., Kållberg, P., Köhler, M., Matricardi, M., McNally, A. P., Monge-Sanz, B. M., Morcrette, J.-J., Park, B.-K., Peubey, C., de Rosnay, P., Tavolato, C., Thépaut, J.-N., and Vitart, F.: The ERA-Interim reanalysis: configuration and performance of the data assimilation system, Quarterly Journal of the Royal Meteorological Society, 137, 553–597, https://doi.org/10.1002/qj.828, 2011.

Diehl, M.: Airborne Wind Energy: Basic Concepts and Physical Foundations, in: Airborne Wind Energy, edited by Ahrens, U., Diehl, M., and Schmehl, R., pp. 3–22, Springer, https://doi.org/10.1007/978-3-642-39965-7_1, 2013.

Donlon, C. J., Martin, M., Stark, J., Roberts-Jones, J., Fiedler, E., and Wimmer, W.: The Operational Sea Surface Temperature and Sea Ice Analysis (OSTIA) system, Remote Sensing of Environment, 116, 140–158, https://doi.org/10.1016/j.rse.2010.10.017, 2012.

Dörenkämper, M., Optis, M., Monahan, A., and Steinfeld, G.: On the Offshore advection of Boundary-Layer Structures and the Influence on Offshore Wind Conditions, Boundary-Layer Meteorol., 155, 459–482, https://doi.org/10.1007/s10546-015-0008-x, 2015.

Dörenkämper, M., Stoevesandt, B., and Heinemann, D.: Derivation of an offshore wind index for the German bight from high-resolution mesoscale simulation data, Proceedings of DEWEK - German Offshore Wind Energy Conference, p. 5, http://publica.fraunhofer.de/documents/N-484817.html, 2017.

Dörenkämper, M., Olsen, B. T., Witha, B., Hahmann, A. N., Davis, N. N., Barcons, J., Ezber, Y., García-Bustamante, E., González-Rouco, J. F., Navarro, J., Sastre-Marugán, M., Sīle, T., Trei, W., Žagar, M., Badger, J., Gottschall, J., Sanz Rodrigo, J., and Mann, J.: The Making of the New European Wind Atlas – Part 2: Production and Evaluation, Geosci. Model Dev. Discuss., 2020, 1–37, https://doi.org/10.5194/gmd-2020-23, 2020.

Echeverri, P., Fricke, T., Homsy, G., and Tucker, N.: The Energy Kite - Selected Results From the Design, Development and Testing of Makani's Airborne Wind Turbines - Part 1, Technical Report, Makani Power, https://storage.googleapis.com/x-prod.appspot.com/files/Makani_TheEnergyKiteReport_Part1.pdf, 2020.

Eijkelhof, D., Rapp, S., Fasel, U., Gaunaa, M., and Schmehl, R.: Reference Design and Simulation Framework of a Multi-Megawatt Airborne Wind Energy System, Journal of Physics: Conference Series, 1618, https://doi.org/10.1088/1742-6596/1618/3/032020, 2020.

Ellis, G. and Ferraro, G.: The Social Acceptance of Wind Energy: Where we stand and the path ahead., EUR - Scientific and Technical Research Reports, European Commission, https://doi.org/10.2789/696070, 2016.

Emeis, S.: Wind energy meteorology : atmospheric physics for wind power generation, Green Energy and Technology, Springer, Berlin Heidelberg, https://doi.org/10.1007/978-3-642-30523-8, 12.02.03; LK 01, 2013.

Fagiano, L. and Milanese, M.: Airborne Wind Energy: An overview, in: 2012 American Control Conference (ACC), pp. 3132–3143, IEEE, https://doi.org/10.1109/ACC.2012.6314801, 2012.

Floors, R., Batchvarova, E., Gryning, S.-E., Hahmann, A. N., Peña, A., and Mikkelsen, T.: Atmospheric boundary layer wind profile at a flat coastal site - wind speed lidar measurements and mesoscale modeling results, Advances in Science and Research, 6, 155–159, https://doi.org/10.5194/asr-6-155-2011, 2011.

Gros, S., Zanon, M., and Diehl, M.: A relaxation strategy for the optimization of airborne wind energy systems, in: Control Conference (ECC), 2013 European, pp. 1011–1016, IEEE, https://doi.org/10.23919/ECC.2013.6669670, 2013.

Haas, T., Schutter, J. D., Diehl, M., and Meyers, J.: Wake characteristics of pumping mode airborne wind energy systems, Journal of Physics: Conference Series, 1256, 012 016, https://doi.org/10.1088/1742-6596/1256/1/012016, 2019.

Hahmann, A. N., Sile, T., Witha, B., Davis, N. N., Dörenkämper, M., Ezber, Y., García-Bustamante, E., González Rouco, J. F., Navarro, J., Olsen, B. T., and Söderberg, S.: The Making of the New European Wind Atlas, Part 1: Model Sensitivity, Geosci. Model Dev. Discuss., 2020, 1–33, https://doi.org/10.5194/gmd-2019-349, 2020.

Hersbach, H. and Dick, D.: ERA5 reanalysis is in production, http://www.ecmwf.int/en/newsletter/147/news/era5-reanalysis-production, last accessed: 2019-10-22, 2016.

Houska, B. and Diehl, M.: Optimal control for power generating kites, in: 2007 European Control Conference (ECC), pp. 3560–3567, IEEE, https://doi.org/10.23919/ECC.2007.7068861, 2007.

HSL: HSL. A collection of Fortran codes for large scale scientific computation, http://www.hsl.rl.ac.uk/, last accessed: 2022-03-14, 2020.

IEC: 61400-1: Design requirements, no. 1,1 in Wind turbines, IEC, Geneva, ed. 3.0, 2010-10 edn., oCLC: 838280539, 2010.

Kruijff, M. and Ruiterkamp, R.: A Roadmap Towards Airborne Wind Energy in the Utility Sector, in: Airborne Wind Energy: Advances in Technology Development and Research, edited by Schmehl, R., pp. 643–662, Springer Singapore, Singapore, https://doi.org/10.1007/978-981-10-1947-0_26, 2018.

Leuthold, R., De Schutter, J., Malz, E., Licitra, G., Gros, S., and Diehl, M.: Operational Regions of a Multi-Kite AWE System, in: 2018 European Control Conference (ECC), pp. 52–57, https://doi.org/10.23919/ECC.2018.8550199, 2018.

Licitra, G.: Identification and optimization of an airborne wind energy system, Ph.D. thesis, University of Freiburg, https://doi.org/10.6094/UNIFR/16226, 2018.

Licitra, G., Koenemann, J., Bürger, A., Williams, P., Ruiterkamp, R., and Diehl, M.: Performance assessment of a rigid wing Airborne Wind Energy pumping system, Energy, 173, 569–585, https://doi.org/10.1016/j.energy.2019.02.064, 2019.

Loyd, M. L.: Crosswind kite power (for large-scale wind power production), Journal of Energy, 4, 106–111, https://doi.org/10.2514/3.48021, 1980.

Lunney, E., Ban, M., Duic, N., and Foley, A.: A state-of-the-art review and feasibility analysis of high altitude wind power in Northern Ireland, Renewable and Sustainable Energy Reviews, 68, 899 – 911, https://doi.org/https://doi.org/10.1016/j.rser.2016.08.014, 2017.

Malz, E., Koenemann, J., Sieberling, S., and Gros, S.: A reference model for airborne wind energy systems for optimization and control, Renewable Energy, 140, 1004 – 1011, https://doi.org/10.1016/j.renene.2019.03.111, 2019.

Malz, E., Hedenus, F., Göransson, L., Verendel, V., and Gros, S.: Drag-mode airborne wind energy vs. wind turbines: An analysis of power production, variability and geography, Energy, 193, 116 765, https://doi.org/https://doi.org/10.1016/j.energy.2019.116765, 2020.

Molina-García, A., Fernández-Guillamón, A., Gómez-Lázaro, E., Honrubia-Escribano, A., and Bueso, M. C.: Vertical Wind Profile Characterization and Identification of Patterns Based on a Shape Clustering Algorithm, IEEE Access, 7, 30 890–30 904, https://doi.org/10.1109/ACCESS.2019.2902242, 2019.

Nakanishi, M. and Niino, H.: Development of an Improved Turbulence Closure Model for the Atmospheric Boundary Layer, Journal of the Meteorological Society of Japan, 87, 895–912, https://doi.org/10.2151/jmsj.87.895, 2009.

Obukhov, A. M.: Turbulence in an atmosphere with a non-uniform temperature, Boundary-Layer Meteorology, 2, 7–29, https://doi.org/10.1007/BF00718085, 1971.

offshorewind.biz: Ampyx Power Taking First Steps Towards MW-Scale Kite, Online, https://www.offshorewind.biz/2018/12/04/ampyx-power-taking-first-steps-towards-mw-scale-kite/, last accessed: 2022-03-14, 2018.

Olauson, J.: ERA5: The new champion of wind power modelling?, Renewable Energy, 126, 322–331, https://doi.org/10.1016/j.renene.2018.03.056, 2018.

Optis, M., Monahan, A., and Bosveld, F. C.: Limitations and breakdown of Monin–Obukhov similarity theory for wind profile extrapolation under stable stratification, Wind Energy, 19, 1053–1072, https://doi.org/10.1002/we.1883, 2016.

Peña, A., Gryning, S.-E., and Floors, R.: Lidar observations of marine boundary-layer winds and heights: a preliminary study, Meteorologische Zeitschrift, 24, 581–589, https://doi.org/10.1127/metz/2015/0636, 2015.

Pedregosa, F., Varoquaux, G., Gramfort, A., Michel, V., Thirion, B., Grisel, O., Blondel, M., Prettenhofer, P., Weiss, R., Dubourg, V., Vanderplas, J., Passos, A., Cournapeau, D., Brucher, M., Perrot, M., and Duchesnay, E.: Scikit-learn: Machine Learning in Python, Journal of Machine Learning Research, 12, 2825–2830, https://doi.org/10.48550/arXiv.1201.0490, 2011.

Salvação, N. and Guedes Soares, C.: Wind resource assessment offshore the Atlantic Iberian coast with the WRF model, Energy, 145, 276 – 287, https://doi.org/https://doi.org/10.1016/j.energy.2017.12.101, 2018.

Schelbergen, M., Kalverla, P. C., Schmehl, R., and Watson, S. J.: Clustering wind profile shapes to estimate airborne wind energy production, Wind Energy Science, 5, 1097–1120, https://doi.org/10.5194/wes-5-1097-2020, 2020.

Schmehl, R., Noom, M., and van der Vlugt, R.: Traction Power Generation with Tethered Wings, in: Airborne Wind Energy, edited by Ahrens, U., Diehl, M., and Schmehl, R., chap. 2, pp. 23–45, Springer, Berlin, Heidelberg, https://doi.org/10.1007/978-3-642-39965-7_2, 2013.

Sempreviva, A. M. and Gryning, S.-E.: Humidity fluctuations in the marine boundary layer measured at a coastal site with an infrared humidity sensor, Boundary-Layer Meteorology, 77, 331–352, https://doi.org/10.1007/BF00123531, 1996.

Skamarock, W., Klemp, J., Dudhia, J., Gill, D., Barker, D., Duda, M., Huang, X., Wang, W., and Powers, J.: A description of the advanced research WRF version 3, Tech. Rep. NCAR/TN–475+STR, NCAR - National Center for Atmospheric Research, Boulder, Colorado, USA, https://doi.org/10.5065/D68S4MVH, 2008.

Skamarock, W. C., Klemp, J. B., Dudhia, J., and Gill, D. O.: A Description of the Advanced Research WRF Model Version 4.3, Technical Report, UCAR, https://doi.org/10.5065/1dfh-6p97, 2021.

Sommerfeld, M., Crawford, C., Monahan, A., and Bastigkeit, I.: LiDAR-based characterization of mid-altitude wind conditions for airborne wind energy systems, Wind Energy, 22, 1101–1120, https://doi.org/https://doi.org/10.1002/we.2343, 2019a.

Sommerfeld, M., Dörenkämper, M., Steinfeld, G., and Crawford, C.: Improving mesoscale wind speed forecasts using lidar-based observation nudging for airborne wind energy systems, Wind Energy Science, 4, 563–580, https://doi.org/10.5194/wes-4-563-2019, 2019b.

Sommerfeld, M., Dörenkämper, M., De Schutter, J., and Crawford, C.: Ground-generation airborne wind energy design space exploration, Wind Energy Science Discussions, 2020, 1–34, https://doi.org/10.5194/wes-2020-123, 2020.

Stull, R.: An Introduction to Boundary Layer Meteorology, Atmospheric and Oceanographic Sciences Library, Springer Netherlands, https://doi.org/https://doi.org/10.1007/978-94-009-3027-8, 1988.

van der Vlugt, R., Bley, A., Noom, M., and Schmehl, R.: Quasi-steady model of a pumping kite power system, Renewable Energy, 131, 83 – 99, https://doi.org/10.1016/j.renene.2018.07.023, 2019.

Waechter, A. and Laird, C.: Ipopt (Interior Point OPTimizer), https://github.com/coin-or/Ipopt, last accessed: 2022-03-14, 2016.

Wächter, A. and Biegler, L. T.: On the implementation of an interior-point filter line-search algorithm for large-scale nonlinear programming, Mathematical Programming, 106, 25–57, https://doi.org/10.1007/s10107-004-0559-y, 2006.

Appendix A: Figures

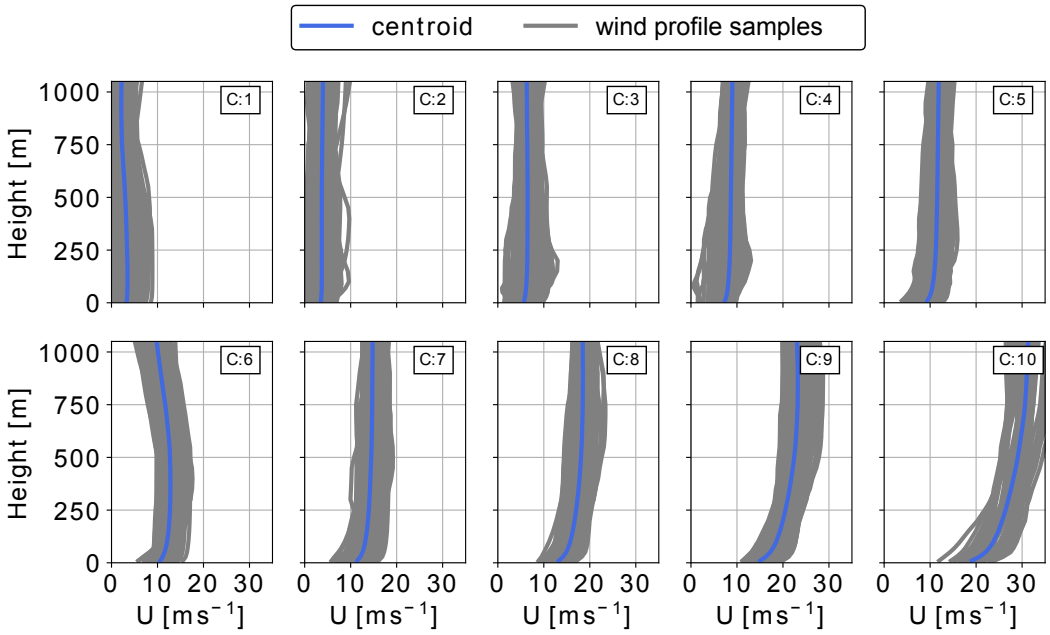

Figure A1. ~~clustered offshore vertical wind velocity profiles (here shown as 2D projected wind speed profiles). The average profile or centroid is shown in blue while all the assigned~~ are shown in grey. Vertical offshore wind velocity profiles (here shown as projected wind speed profiles) categorized into $k = 10$ clustered using the k-means clustering algorithm. The average profile (centroid) is shown in blue and the profiles associated with this cluster are shown in grey. The clusters are sorted and labeled in ascending order of average centroid wind speed up to 500 m. The corresponding cluster frequency f for each cluster C is shown in Figure 5

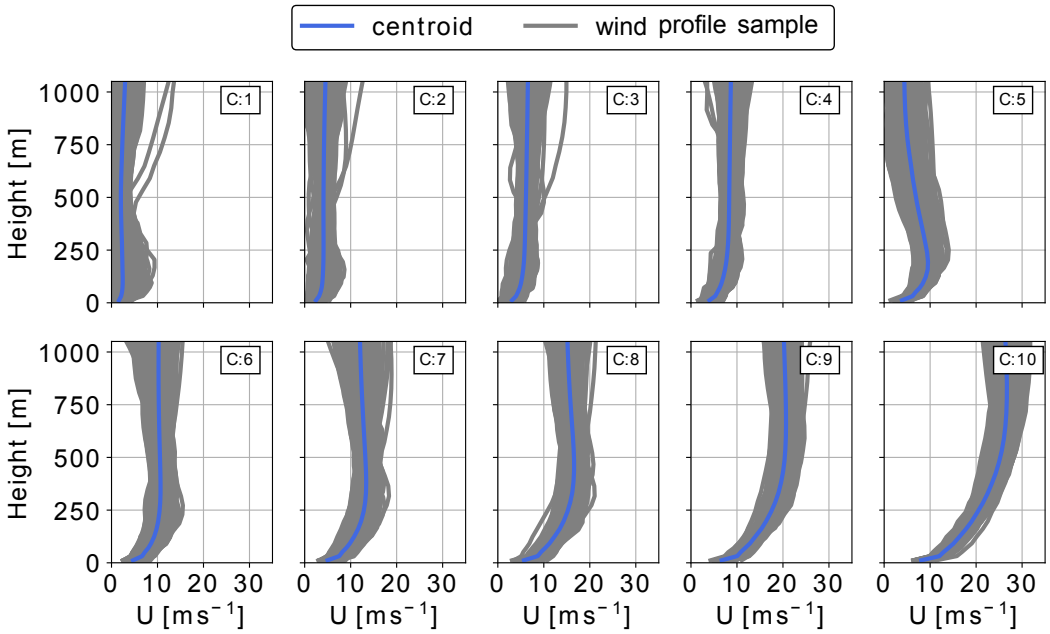

Figure A2. ~~Clustered onshore wind velocity profiles (here shown as wind speed profiles). The average profile or centroid is shown in blue while all the assigned profiles are shown in grey.~~ Vertical onshore wind velocity profiles (here shown as projected wind speed profiles) categorized into $k = 10$ clustered using the k-means clustering algorithm. The average profile or centroid is shown in blue while the profiles associated with this cluster are shown in grey. The clusters are sorted and labeled in ascending order of average centroid wind speed up to 500 m. The corresponding cluster frequency f for each cluster C is shown in Figure 5

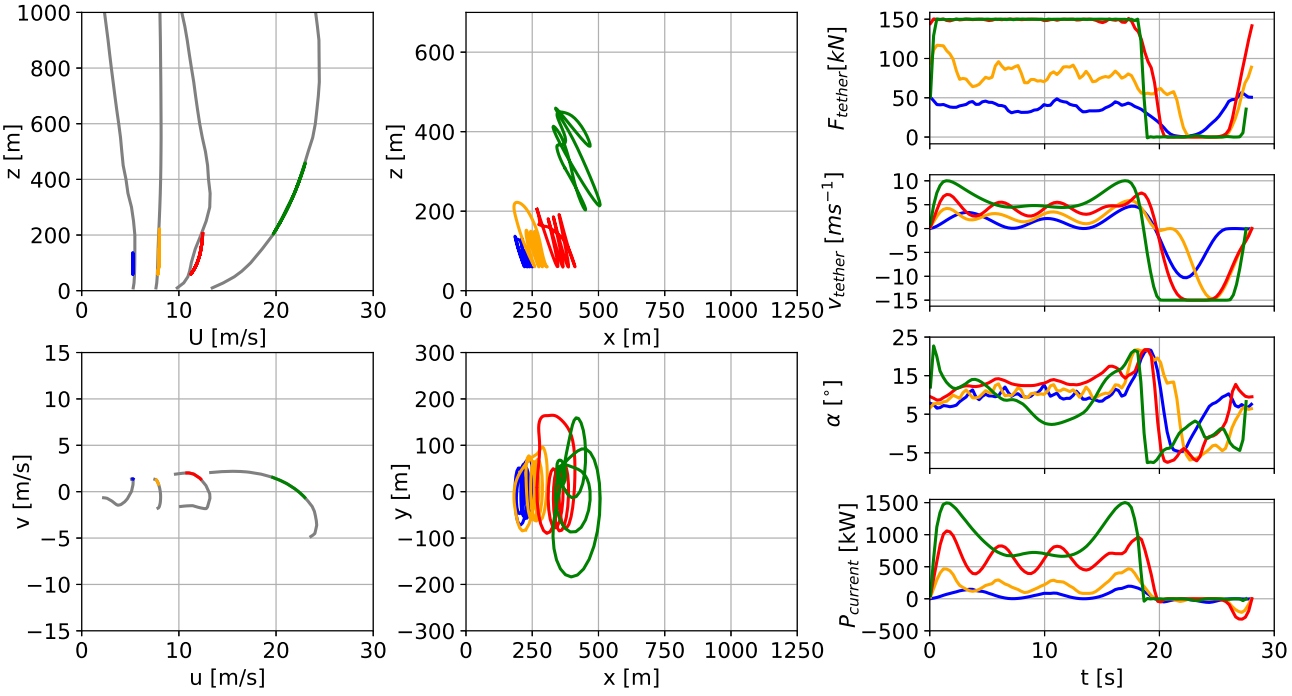

Figure A3. ~~Representative wind speed profiles (a), and hodograph (top view) of wind velocity up to 1000 m (c). The deviation of the colored lines is caused by the approximation of discrete data points with Lagrange polynomials. Trajectories (b,d) in side and top view. Temporal variations of tether force F_{tether} (e), tether speed v_{tether} (f), angle of attack α (g) and instantaneous power P_{current} (h) optimized based on clustered offshore wind speed profiles for a ground-generation aircraft with a wing area of $A_{\text{wing}} = 20\ \text{m}^2$.~~

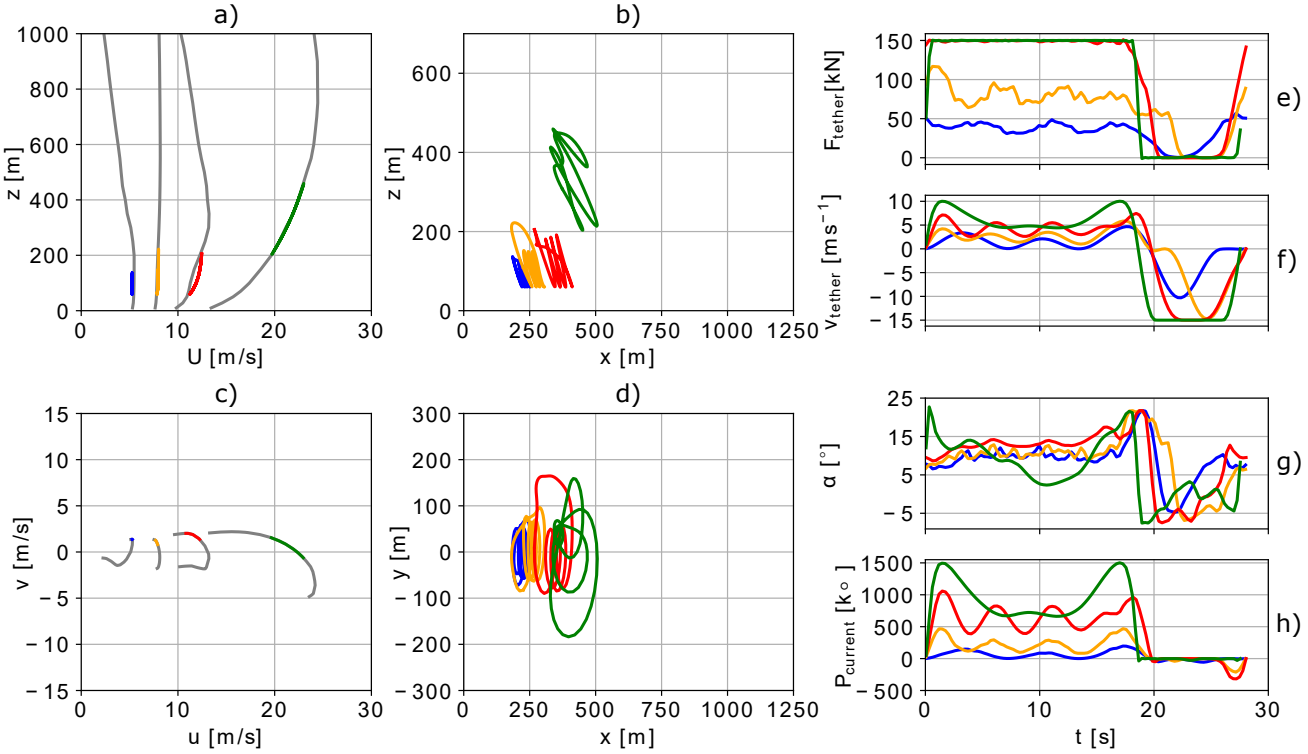

Figure A4. Representative wind speed profiles (a), and hodograph (top view) of wind velocity up to 1000 m (c). The deviation of the colored lines is caused by the approximation of discrete data points with Lagrange polynomials. Trajectories (b,d) in side and top view. Temporal variations of tether force F_{tether} (e), tether speed $v_{\text{tether}}\dot{l}$ (f), angle of attack α (g) and instantaneous power P_{current} (h) optimized based on clustered offshore wind speed profiles for a ground-generation aircraft with a wing area of $A_{\text{wing}} = 20\ \text{m}^2$.